Additive Manufacturing 94 (2024) 104449

Contents lists available at ScienceDirect

Additive Manufacturing

journal homepage: www.elsevier.com/locate/addma

A heterogeneous pore design algorithm for material extrusion additive manufacturing

Huawei Qu [a], Kaizheng Liu [a,b], Juan Liu [a], Chongjian Gao [a], Changshun Ruan [a,b,*]

[a] Research Center for Human Tissue and Organ Degeneration, Institute of Biomedicine and Biotechnology, Shenzhen Institute of Advanced Technology, Chinese Academy of Sciences, Shenzhen 518055, China
[b] University of Chinese Academy of Sciences, Beijing 100049, China

ARTICLE INFO

Keywords:
Additive manufacturing
Material extrusion
Heterogeneous design
Gradient porous structures
Parametric algorithm

ABSTRACT

Material extrusion additive manufacturing offers great potential for customizing matters with complex external contours, and filament diameter-adjustable 3D (FDA-3D) printing strategy provides fresh impetus to create heterogeneous porous structures inside these complex matters. However, the absence of supporting algorithms to implement FDA-3D printing severely hinders its widespread use. In this paper, we develop a heterogeneous pore design (HPD) algorithm aimed at advancing the development of FDA-3D printing for producing heterogeneous porous matters. The HPD algorithm consists of three sub-algorithms: model design, collapse compensation, and fabrication file (G-codes) generation. As proofs of concept, we utilize this algorithm to 3D print radial gradient and letter-embedded gradient materials following specific steps: (1) designing the heterogeneous porous models with collapse compensation in Grasshopper® and displaying them in Rhinocores®; (2) customizing and writing the corresponding G-codes files by following the material extrusion 3D printer's control rules; (3) upgrading a commercial extrusion printer to FDA-3D print the design models via the customized G-codes. Micro-computed tomography-based 3D reconstruction and quantified pore size maps for the fabricated objects demonstrate the high capability of this HPD algorithm. Overall, the HPD algorithm holds the potential to revolutionize material extrusion 3D printers cost-effectively, creating new possibilities for material extrusion of heterogeneous materials.

1. Introduction

Heterogeneity imparts distinctive properties to natural materials, attributable to their spatial hierarchy, including pore gradients [1,2]. For example, human bone is composed of loose, porous cancellous bone and dense, less porous cortical bone [3]. The former provides space for blood vessels and nerves to survive, and the latter offers mechanical support to the body [4]. Hence, fabricating heterogeneous materials with an internal gradient porous structure is essential to realize customized functions in diverse applications.

The rapid development of additive manufacturing, commonly known as three-dimensional (3D) printing, presents an innovative avenue for building complex objects. Material extrusion 3D printing, encompassing techniques such as direct ink writing and fused deposition molding [5–9], stands as one of the most widely employed AM methods across various fields [10,11], including flexible electronics [12,13], soft robotics [14–17], functional materials [18–20], tissue-engineered scaffolds [21–24], concrete buildings [25,26], 4D printed devices [27,28], and artificial foods [29–31]. Despite offering robust support for producing samples with complex external contours, challenges persist in creating internal heterogeneous pore structures due to their uniform pattern-filling strategy with constant filament diameters [32,33]. The

Abbreviations: FDA, Filament diameter-adjustable; 3DP, Three dimensional or three-dimensional printing; CAD, Computer-aided design; G-codes, Fabrication file for extrusion 3D printers; ROI, Region of interest; Micro-CT, Micro-computed tomography; Q, Flow rate of ink extruded from the nozzle; V, Printing velocity in FDA-3DP process, nozzle moving relative to the substrate; H, Printing height in FDA-3DP process, from nozzle outlet to the substrate; L, Spacing between parallel printing path or trajectory; S, Area of oblong filament cross-section; D, Filament mathematical diameter, from $D = 4S/\pi^{0.5}$; w,, Width of oblong filament cross-section; h, Height of oblong filament cross-section; AR, Aspect ratio of oblong filament cross-section, from $AR = w/h$; d, Pore size between parallel filaments, from $d = L\text{-}w$.

* Corresponding author at: Research Center for Human Tissue and Organ Degeneration, Institute of Biomedicine and Biotechnology, Shenzhen Institute of Advanced Technology, Chinese Academy of Sciences, Shenzhen 518055, China.
E-mail address: cs.ruan@siat.ac.cn (C. Ruan).

https://doi.org/10.1016/j.addma.2024.104449
Received 8 May 2024; Received in revised form 19 September 2024; Accepted 21 September 2024
Available online 25 September 2024

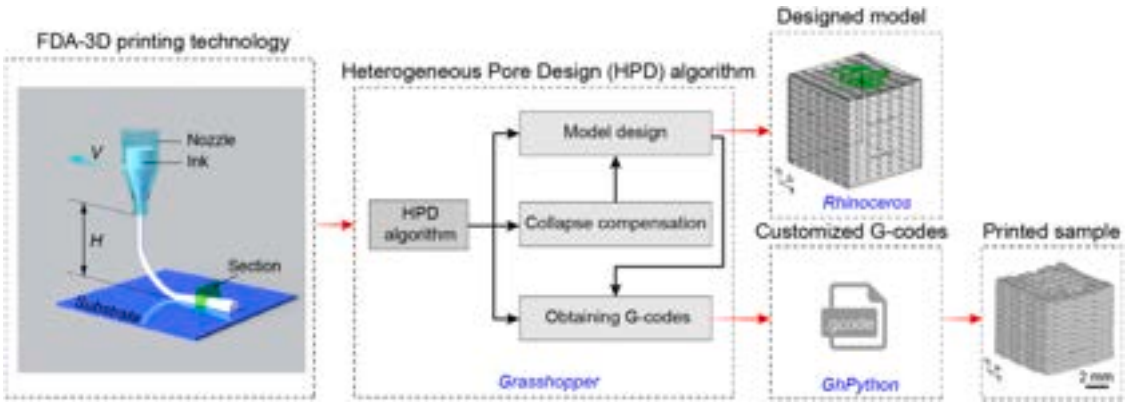

Fig. 1. Workflow from FDA-3D printing technology to model design, model visualization and sample fabrication. The HPD algorithm was developed based on FDA-3D printing technology. It consists of three sub-algorithms: model design, collapse compensation, and obtaining G-codes.

previous literature indicates that adjusting the printing velocity is an accepted strategy for producing filaments with variable cross sections or widths [34–38]. In response to these challenges, we have previously developed filament diameter-adjustable 3D (FDA-3D) printing with tunable filling density [39]. This technique precisely regulates the number of inks deposited on the printing path, offering a novel approach to creating internal heterogeneous structures with tunable gradients.

Nevertheless, to our knowledge, existing model slicing and trajectory planning algorithms (e.g., Cura, PrusaSlicer, and Simplify3D) for material extrusion 3D printing were primarily designed for uniform pores [40,41]. Consequently, extending them to support the non-uniform fiber-filling strategy of FDA-3D printing proves challenging. As such, it is extremely critical to establish a standardized and high-performance algorithm to enable the FDA-3D printing of heterogeneous matters for conventional material extrusion 3D printers.

In this study, we introduced a heterogeneous pore design (HPD) algorithm, aiming to design and preview gradient porous models without collapse. Additionally, this HPD algorithm can be used to upgrade conventional extrusion printers with G-codes to perform FDA-3D printing of the designed models at low cost, as depicted in Fig. 1. In short, the HPD algorithm has three functions: (1) model design, (2) collapse compensation, and (3) generation of G-code files. The software platform for implementing this algorithm is the modeling software Rhinoceros® coupled with the parametric tool Grasshopper® (Robert McNeel & Associates, United States). The Grasshopper® was used to develop the entire HPD algorithm, while the Rhinoceros® is only used to display the final designed model. The hardware platform used in this paper is a commercial pneumatic extrusion-based 3D printer (Regenovo Bio-Architect® WS, China). G-code files, generated by the Grasshopper's built-in battery GhPython Script, served as a bridge from parametric HPD modeling to sample fabrication. Quantitatively, the high performance of this algorithm was demonstrated through the high-fidelity geometry and a high-agreement porous gradient observed between the fabricated samples and the design models. In all, we anticipate that the HPD algorithm could find applications in a diverse range of material extrusion scenarios for gradient porous structures.

2. Material and methods

2.1. Ink preparation

Polycaprolactone (PCL) with an average molecular weight (Mn) of 45,000 was purchased from Aldrich Inc. β-tri-calcium phosphate (β-TCP) was obtained from Sigma-Aldrich Inc. A 4:1 wt ratio of PCL and β-TCP, without any modification, underwent heating in a beaker at 110°C for 30 minutes. The mixture was stirred with a glass rod, repeating these steps five times. The blended material was transferred to our laboratory's pneumatic-based 3D printer with a nozzle diameter of 400 μm. It was then held at 110°C for 30 minutes before initiating 3D printing.

2.2. Software platform

The CAD software Rhinoceros® (v7 SR18, https://www.rhino3d.com) and its parametric tool Grasshopper® (https://www.grasshopper3d.com) served as the software platform for implementing our proposed algorithm in this study. Parametric modeling of heterogeneous pore structures was carried out in Grasshopper® using various inbuilt batteries such as Line, Join Curves, Loft, Cap Holes, Solid Intersection, Anemone, and GhPython Script. For visualization, the designed 3D models were baked out from Grasshopper® to Rhinoceros®.

2.3. Hardware platform

The material extrusion-based 3D printer (Regenovo Bio-Architect® WS) and its accompanying control software (3D Bio-Architect®) were purchased from Hangzhou Regenovo Biotechnology Co., LTD. The Regenovo printer was selected as the hardware platform for this study. The Regenovo software was used to initialize the extrusion printer (hardware platform) before 3D printing. Additionally, it was employed to call and execute the fabrication files (G-codes) generated by our proposed algorithms.

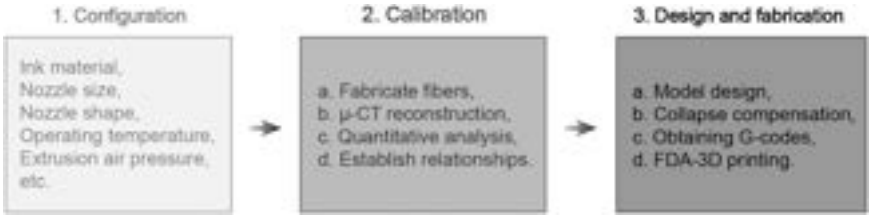

Fig. 2. Workflow of the HPD algorithm.

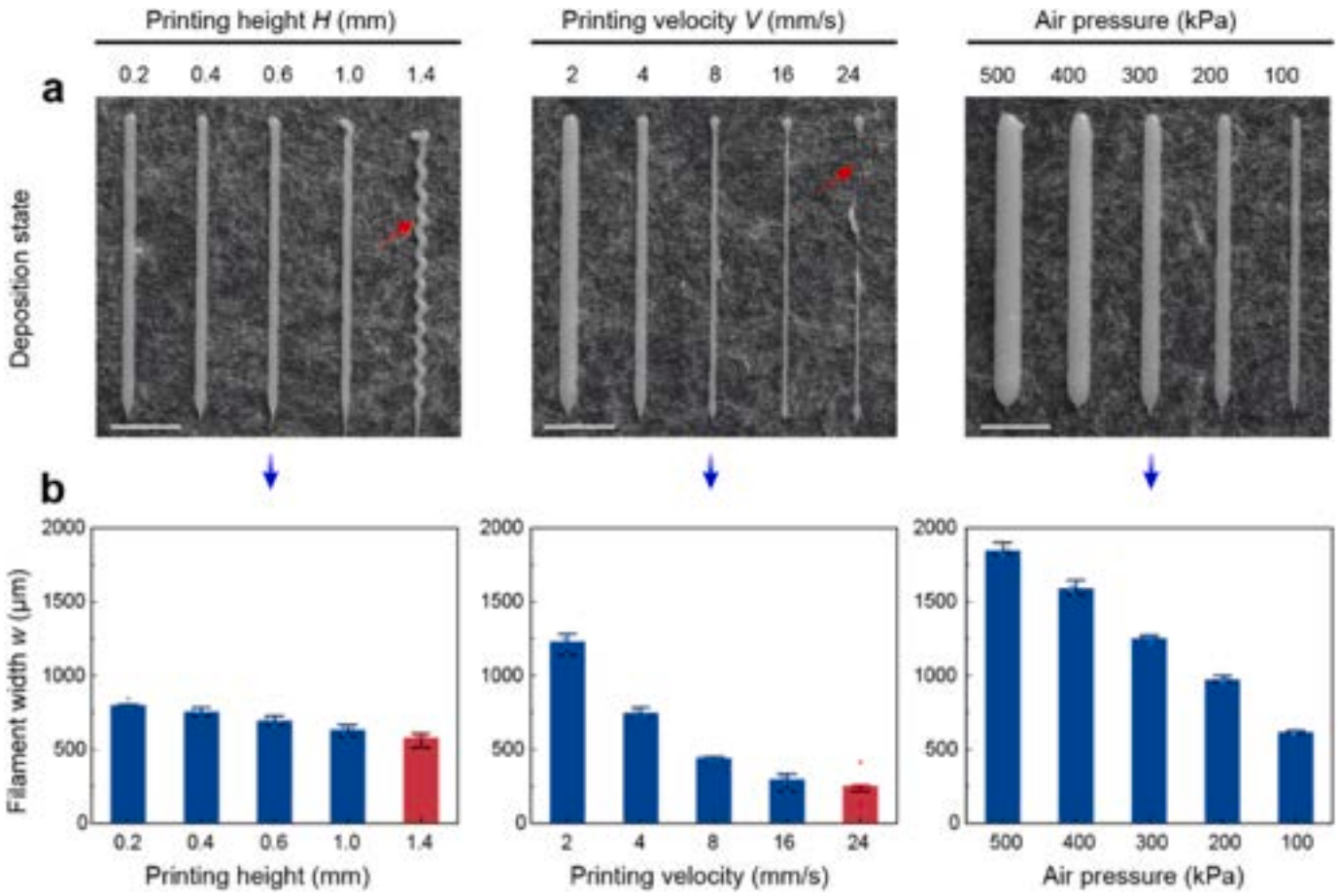

Fig. 3. Filament deposition states (a) and cross-sectional widths *w* (b) at different printing parameters. 20 mm-long single-filament samples were used to evaluate the filament deposition states. Quantitative *w* was obtained from top-view optical images using the software ImageJ. Each data has six replicates (n=6). The blue and red columns indicate the acceptable and unacceptable deposition status, respectively. The unacceptable states are the coiled rope effect (left) and material discontinuity (middle), respectively. Scale bar, 5 mm.

2.4. Algorithmic foundation

2.4.1. Algorithmic workflow

The workflow of the HPD algorithm consists of three steps: 1. Configuration, 2. Calibration, and 3. Design and fabrication, as depicted in Fig. 2. First of all, work factors such as ink material, nozzle size, nozzle shape, operating temperature, extrusion air pressure, etc. are determined and configured according to the target project. Notice that the printing velocity *V* and printing height *H* are customized and varied in this work.

Then, in the Calibration section, we perform the following:

a. Fabricating 50 mm-long fiber segments at uniformly varying print speeds;
b. Perform CT scanning of the fabricated parts and reconstruct the 3D models;
c. Quantitatively evaluate the reconstructed 3D models for fiber cross-sectional area and aspect ratio using ImageJ;
d. Establishing the printing velocity *V* as a function of fiber cross-sectional area *S* and aspect ratio *AR*.

Finally, in the Design and fabrication section, the following operations are implemented:

a. Following sub-algorithm 1, perform the design of the gradient porous model;
b. Following sub-algorithm 2, implement the automatic compensation of collapse;
c. Following sub-algorithm 3, complete the availability of customized fabrication codes (G-codes);
d. Execute the G-codes to program and perform FDA-3D printing.

Table 1
Printing parameters for Fig. 3.

Location	Extrusion air pressure (kPa)	Printing velocity (mm s^{-1})	Printing height (mm)
Left	500	4	0.2, 0.4, 0.6, 1.0, and 1.4
Middle	500	2, 4, 8, 16, and 24	0.3, 0.3, 0.3, 0.3, and 0.2
Right	500, 400, 300, 200, and 100	1	0.3, 0.3, 0.2, 0.1, and 0.1

2.4.2. Algorithmic details

During 3D printing, to precisely control the amount of deposited ink on print paths, we investigated the relationship between printing parameters and filament deposition states, as shown in Fig. 3. The detailed parameters used in this investigation are shown in Table 1. This work employs a pneumatic-driven material extrusion 3D printer. The extrusion air pressure is applied to the extruder. To reduce experimental costs, we chose filament cross-sectional width (*w*) to represent filament mathematical diameter *D* due to a positive correlation between them [39]. *D* is derived from the filament cross-sectional area *S* using Eq. 1.

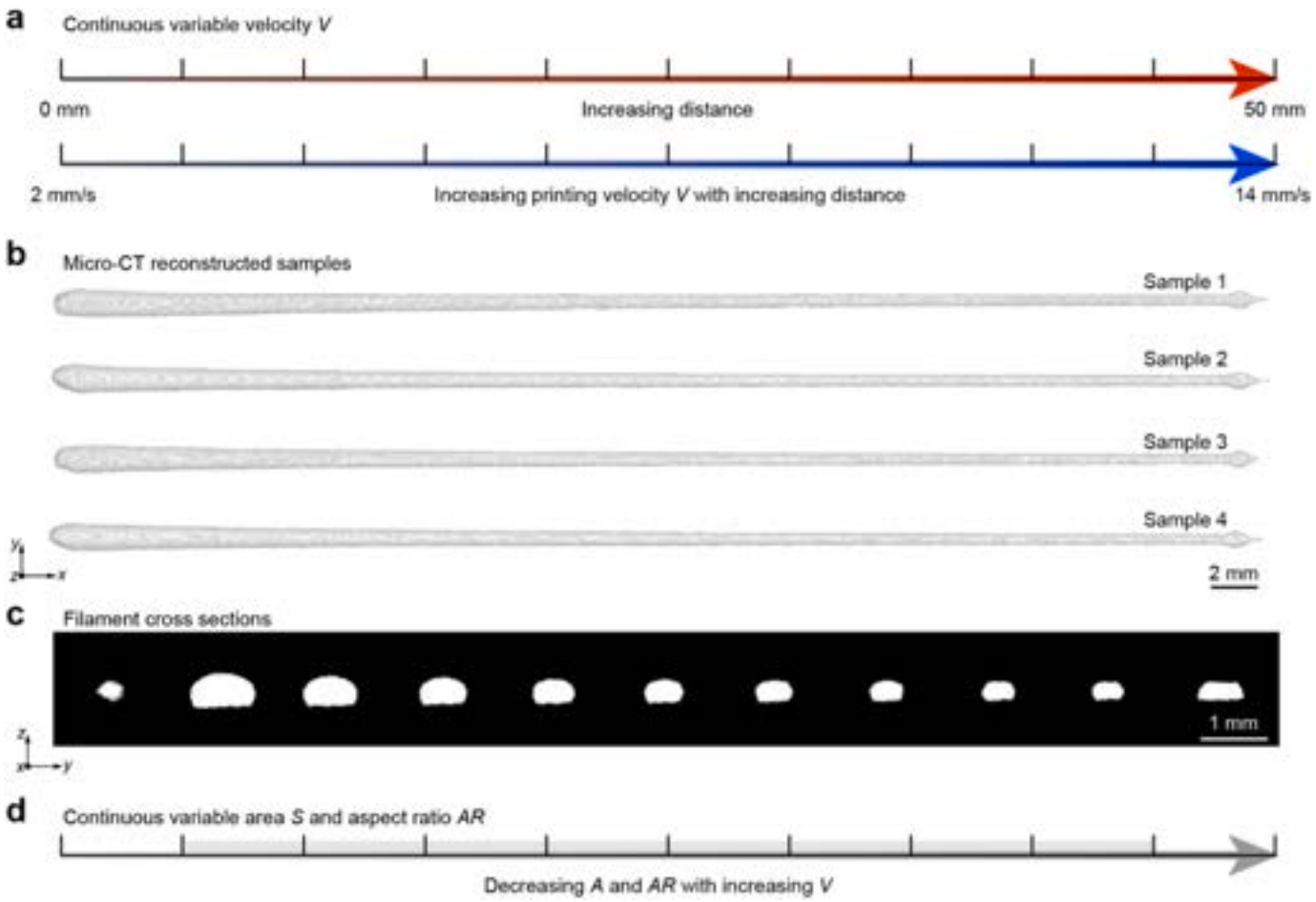

Fig. 4. Single-filament samples with continuous variable cross-sectional sizes. (a) Variable V from 2 mm s^{-1} to 14 mm s^{-1} on a 50 mm-long printing trajectory. (b) Top view of micro-CT reconstructed samples. (c) Cross sections of micro-CT reconstructed samples. (d) Qualitative evaluation of gradient decrease in S and AR with increasing V in the region of interest (ROI). ROI marked in gray was chosen to avoid interference with the cross-section shape by material stacking at the printing start and end positions.

$$D = \sqrt{4S/\pi} \tag{1}$$

After identifying that printing velocity deterministically influences the amount of deposited ink, we explored the relationship between printing velocity and filament cross-sectional size. This section was developed to establish a parametric basis for the design of heterogeneous pore structures. In this section, we focused on single filaments with variable cross-sectional sizes and designed a 50 mm-long printing path with uniformly varying velocities (from 2 to 14 mm s^{-1}). Top views (Fig. 4b) and cross-sectional views (Fig. 4c) of micro-CT reconstructed samples showed that the continuous variation in printing velocity successfully drove the manufacturing of variable diameter filaments based on FDA-3D printing technology. To improve the reliability of experimental data, we kept only region of interest (ROI) data that had uniform variation in filament cross-sections by removing the start and end data (Fig. 4). The filament cross-sectional size consists of w, h, S, and AR, where AR is w divided by h (Eq. 2) and S is constructed from w and h (Eq. 3).

$$AR = w/h \tag{2}$$

$$S = (w-h)\times h + \left(\frac{h}{2}\right)^2 \times \pi \tag{3}$$

Fig. 5a and c demonstrated S and AR of four 50 mm-long single-filament samples, respectively. Their data points in ROI were selected (Fig. 5b and d) and further fitted (Eqs. 4 and 5).

$$S = 1.310 \times V^{-1} \tag{4}$$

$$AR = 2.161 \times V^{-0.111} \tag{5}$$

The fitting result of S (Eq. 4) was in good agreement with its theoretical one derived through fluid flow (Eq. 6) [7].

$$S = Q \times V^{-1} \tag{6}$$

where Q is the flow rate of extruded ink through the nozzle. According to Eqs. 2–5, w and h could be obtained after determining V.

Further, we investigated the design of heterogeneous porous structures. Specifically, FDA-3D printing was based on the law of volume conservation. As the material volume increased, the pore size d would decrease. In our design, the filament cross-sectional shape was approximated to be oblong, and the pore size d was calculated as shown in Eq. 7.

$$d = L - w \tag{7}$$

where d is the pore size between fixed-spacing filaments, L is the spacing between parallel printing trajectories, and w is the cross-sectional width of filaments (Fig. 6b).

2.5. Rules for G-codes

The Regenovo printer's fabrication G-code file format is *.gcode.

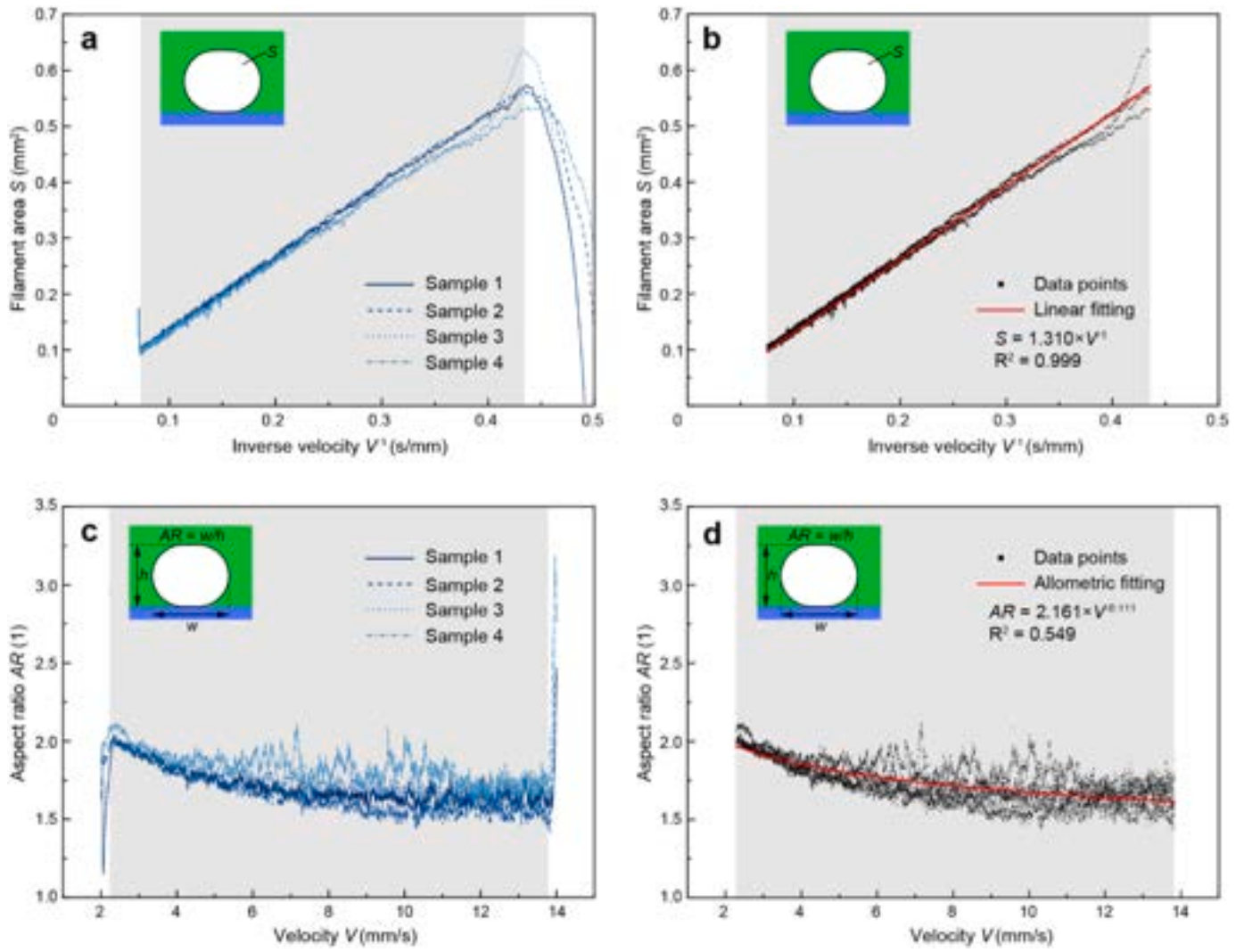

Fig. 5. Building the relationship of V versus S and V versus AR, respectively. Four parallel sample data for V versus S (a) and V versus AR (c) are shown, respectively. Their data points in ROI (marked in gray) were used for function fitting, as shown in (b) and (d), respectively.

Specifically, the G-code file consists of three sections: start, main, and end sections. The start section includes device initialization and setting printing parameters such as extrusion air pressure and advance times for shut-on and shut-off. The main section includes switching the ink feeding and a series of moving commands. Each line begins with 'G1' and is followed by a series of moving points and their corresponding printing velocities, such as G1 X1.1 Y2.2 Z3.3 F6. The end section is to control the 3D printer's nozzle back to the home position. Note that text can be added inside parentheses for comments.

2.6. Writing G-codes

Details of the extrusion 3D printer, ink, and work settings used in this study are shown in Table 2. To generate fabricate files (G-codes), a series of moving points (pts_i) and printing velocities (V_i) corresponding to the FDA and supporting layers were input into GhPython. In addition, data types and statistics related to the above were also input to the sub-algorithm 3 (Fig. 17), such as $line_j$., N_pts, N_line, N_layer, $Bool_k$, N_line_k, $N\_pts\_sup_{k\text{-}m}$, and $pts\_sup_{k\text{-}m\text{-}n}$. Notably, at the end of the ink deposition for each filament, an 8 mm-long nozzle movement without feed along the current direction was set to complete the filament break, which facilitated the smooth start of the next filament printing.

2.7. Heterogeneous pore design

Based on the relationship between V and filament cross-sectional size (Eqs. 2–5, Material and Methods), Fig. 6a illustrates the design steps of a single-layer model with a radial gradient in pore sizes. First, we drew a quantitative map of pore size distribution satisfying the radial requirement. The pore size d was calculated using Eq. 7 (Material and Methods), as shown in Fig. 6b. All pixels in this map had a defined pore size value $\{d_1, \ldots, d_n\}$, where d_o is both the origin data and the maximum pore size d_{max}. The distance relationship between d_o and $\{d_1, \ldots, d_n\}$ was established in the x-y coordinate plane, denoted as $[d_o \sim \{d_1, \ldots, d_n\}]$. Second, the moving points $\{P_1, \ldots, P_n\}$ were extracted on a grid trajectory at a $\leq$0.4 mm fabrication resolution [39], where P_o is the origin point. The z-coordinates of all moving points are the same and greater than h_{max} (z-coordinate $> h_{max}$), where h_{max} is the maximum value in all filament cross-sectional heights (h) used in this work. The distance relationship between P_o and $\{P_1, \ldots, P_n\}$ was established in the x-y coordinate plane, denoted as $[P_o \sim \{P_1, \ldots, P_n\}]$. Third, the target pore sizes and the grid trajectory were merged, and then P_o was moved to the position of d_o in the x-y coordinate plane. By one-to-one mapping of the two distance relationships $[d_o \sim \{d_1, \ldots, d_n\}]$ and $[P_o \sim \{P_1, \ldots, P_n\}]$, a series of pore sizes matching all moving points were obtained. On this basis, filament cross-sectional widths $\{w_1, \ldots, w_n\}$ and heights $\{h_1, \ldots, h_n\}$ (Fig. 6c) matching all moving points were accessed using Eqs. 2–7 (Material and

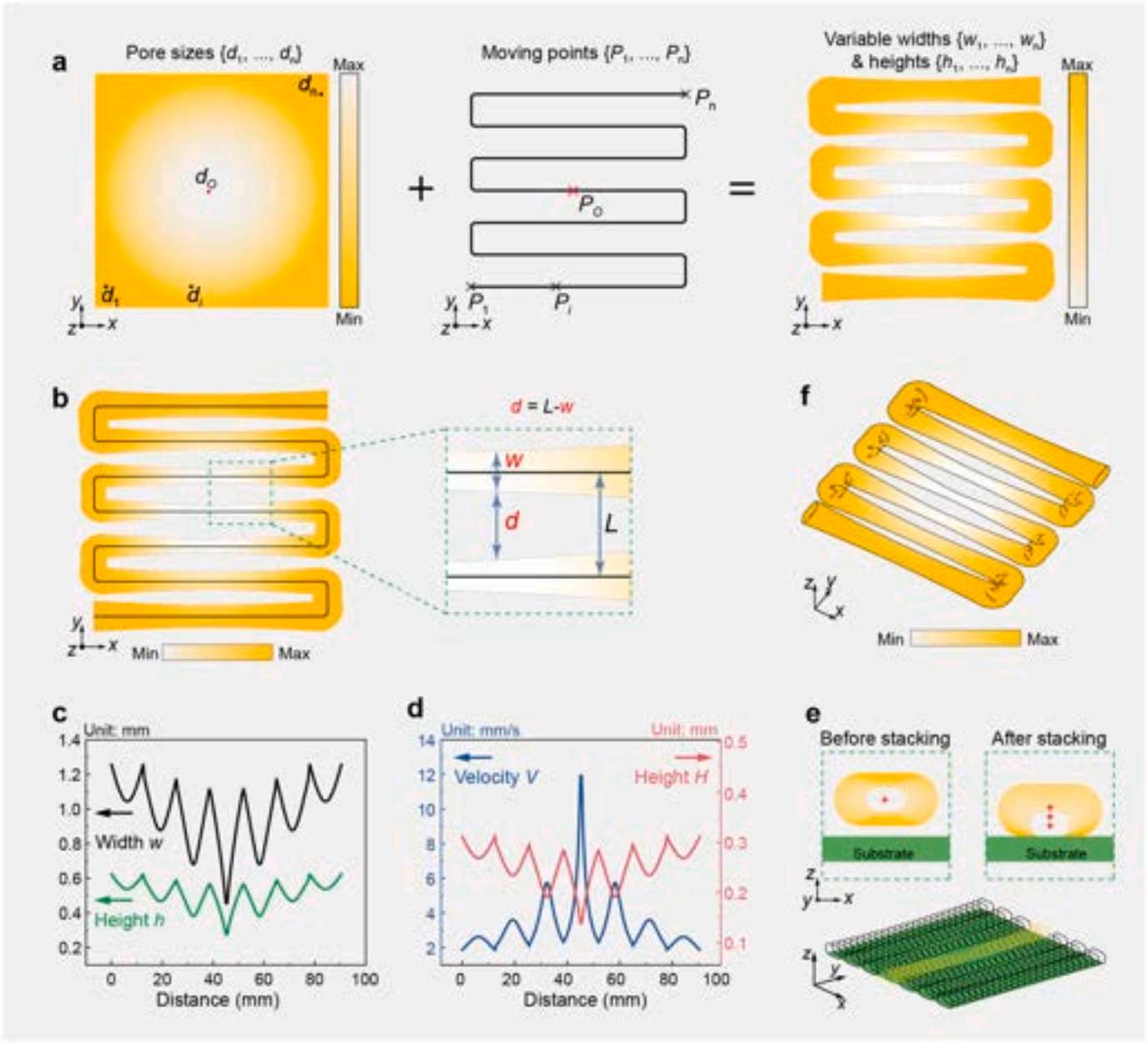

Fig. 6. Schematic illustration of heterogeneous pore design for a single-layer model, selecting a radial gradient as an example. (a) Establishing the relationship between gradient pore sizes $\{d_1, \ldots, d_n\}$ and the widths $\{w_1, \ldots, w_n\}$ and heights $\{h_1, \ldots, h_n\}$ of oblong filaments via mapping. In (a), the left and right pseudo-colors represent the pore size and structure size, respectively. The middle black line represents the print trajectory composed of a series of moving points. (b) Definition of pore size between adjacent filaments within a single layer (Eq. 7, Material and Methods). The pseudo-color indicates structure size, and the green dashed square on the right represents the enlarged schematic. (c) Filament cross-sectional widths $\{w_1, \ldots, w_n\}$ and heights $\{h_1, \ldots, h_n\}$ of a single-layer model. (d) Printing heights H and velocities V of a single-layer model. (e) A series of closed curves onto the substrate before and after stacking. The bottom subfigure shows the closed curves for the single-layer filament after moving. (f) Designed a single-layer filament 3D model showing a radial gradient in structure size. The pseudo-color indicates structure size.

Table 2
The equipment, material, and settings used in this work.

3D printer	Extrusion air pressure	Printing material	Nozzle inner diameter	Heating temperature
Regenovo Bio-Architect® WS	550 kPa	PCL/β-TCP	400 μm	110 ℃

Methods) based on the obtained a series of pore sizes. Also, we obtained a series of V (blue, Fig. 6d) matching the moving points on the grid trajectory. Since the filament cross-sectional shape was approximated as oblong, $\{w_1, \ldots, w_n\}$ and $\{h_1, \ldots, h_n\}$ produced a series of closed curves with the same z-coordinates (upper left sub-figure, before stacking, Fig. 6e). To simulate filament deposition, the produced closed curves were moved and stacked onto the substrate (upper right and lower sub-figure, after stacking, Fig. 6e), obtaining new moving points with variable z-coordinates (i.e., H) (red, Fig. 6d) and new printing trajectory. V and H (Fig. 6d) were used for writing G-codes and FDA-3D printing. Further, the new closed curves onto the substrate were lofted along the new printing trajectory, and thus were capped to obtain the single-layer filament 3D model with a radial gradient in structure sizes (Fig. 6f).

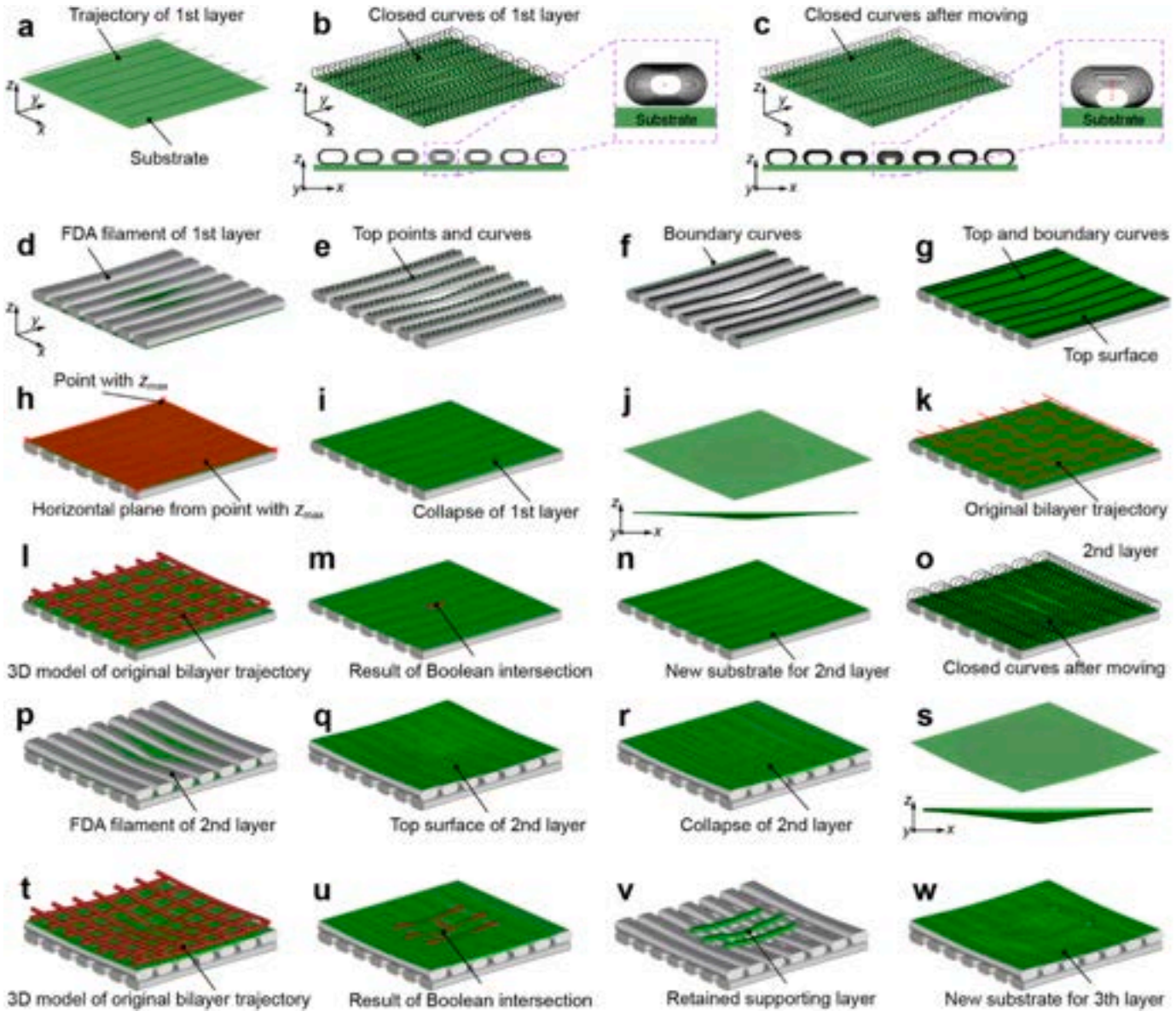

Fig. 7. Steps for collapse compensation.(a) Original trajectory curves for the first FDA layer. (b) Closed curves of the first FDA layer designed based on the pore size requirement and Eqs. 1–6. The centers of these closed curves have the same *z*-height. (c) Stacking the closed curves onto the substrate. The centers of the moved curves are lined up to create a new printing trajectory for the current FDA layer. (d) Lofting and then capping the closed curves to build the 3D models of the first FDA layer. (e) Extracting the centers of the top segments of the closed curves and linking them into curves (named top curves). (f) Moving the first and last curves obtained in (e) to the two boundaries of the square, respectively. The moved curves are named boundary curves. (g) Creating the top surface of the first FDA layer based on the top and boundary curves obtained in (e-f). (h) Selecting the highest point of the top surface and then using it to create a horizontal plane marked in red. (i) Modeling the collapse of the first FDA layer between the top surface and the horizontal plane. (j) 3D view (top sub-figure) and front view (bottom sub-figure) of the collapse of the first FDA layer. (k) Stacking an original bilayer (top and bottom layers) trajectory on the top surface. The vertical distances from the moving points to the top plane for the top and bottom layer trajectories are h_{max} and $2\times h_{max}$, respectively. (l) Piping the stacked bilayer supporting filaments with constant w_{min} and h_{min}. (m) Boolean intersection operation result for the first FDA layer. Only filaments produced with a length of more than 3 mm are reserved for the supporting layers. (n) Selecting the top surface obtained from (g) as a new substrate for the second FDA layer. (o) Stacking the closed curves of the second FDA layer onto the new substrate. (p) Building the 3D model of the second FDA layer. (q) Creating the top surface of the second FDA layer. (r) Modeling the collapse of the second FDA layer. (s) 3D view (top sub-figure) and front view (bottom sub-figure) of the collapse of the second FDA layer. (t) Piping the stacked bilayer supporting filaments with constant w_{min} and h_{min} for the second FDA layer. (u) Boolean intersection operation result for the second FDA layer. (v) The retained supporting layer for the second FDA layer. (w)Creating the top surface of the second FDA layer after stacking the supporting layer.

2.8. Support generation for collapse prevention

As illustrated in Fig. 7, the steps of collapse compensation for a two-layer model are shown as follows:

The sub-figures (a-w) mentioned in this section are all in Fig. 7.

Step 1. The closed curves of the first FDA layer were moved and stacked onto the substrate, and then were lofted and caped into 3D models (a-d).

Step 2. The top surface of the resulting model was extracted (e-g), and the horizontal surface of the first layer was created based on the top surface (h). Further details were described in the figure legend.

Step 3. The collapse (i-j) was constructed by offsetting and stretching the top surface and horizontal plane obtained from Step 2.

Step 4. Boolean intersection operation was implemented between

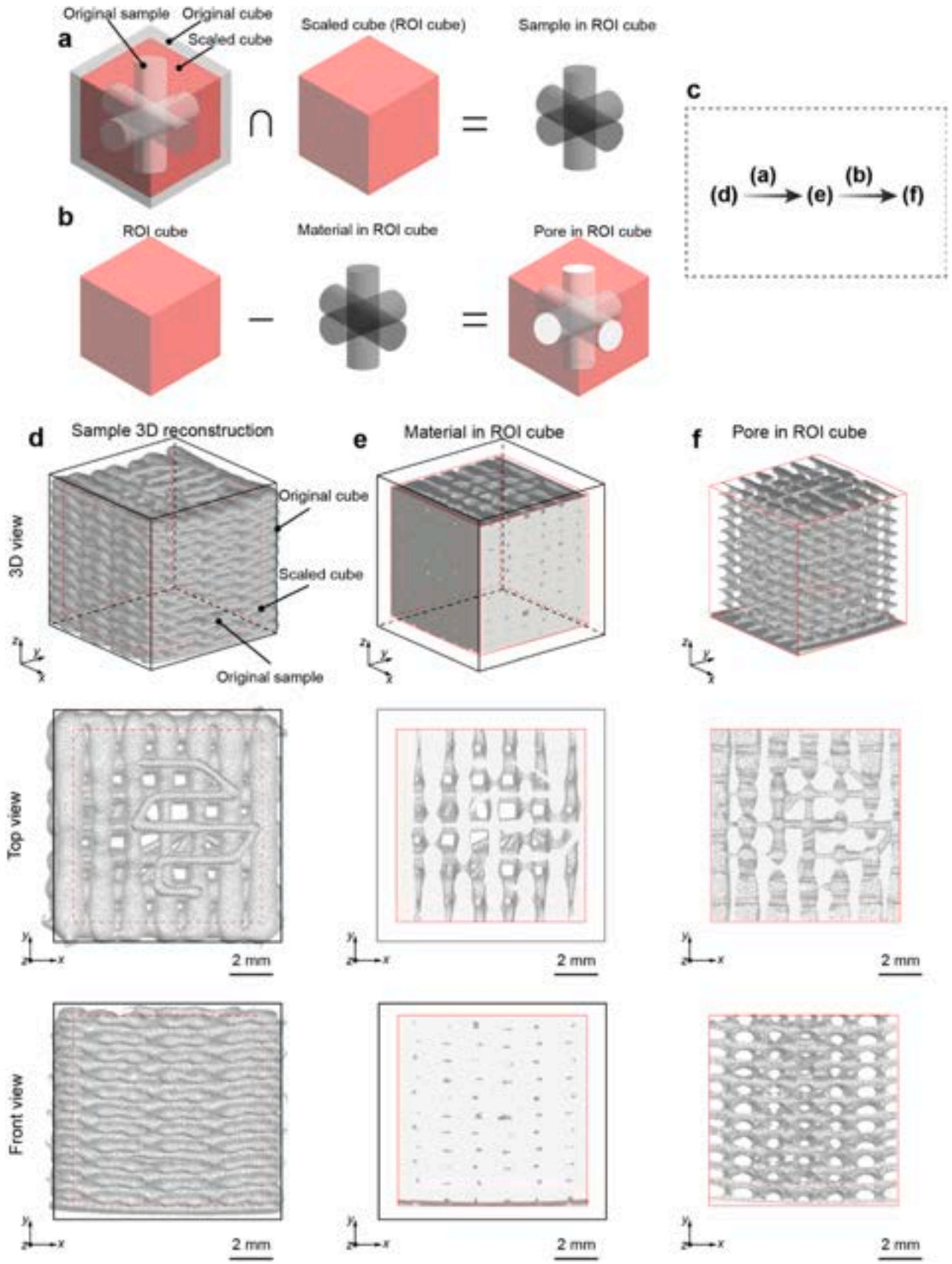

Fig. 8. Two-step Boolean operation for obtaining the pore structure image dataset. (a) Boolean intersection operation between the original sample (about $10\times10\times10$ mm^3) and the scaled cube (ROI, about $9\times9\times9$ mm). (b) Boolean subtraction operation between the ROI cube and the sample material. (c) Schematic of the two-step Boolean operation. (d) Sample 3D reconstruction based on micro-CT. (e) Sample material in the ROI cube. (f) Pore in the ROI cube. Scale bar, 2 mm. In (d-f), the 3D view, top view, and front view of the heterogeneous model are displayed.

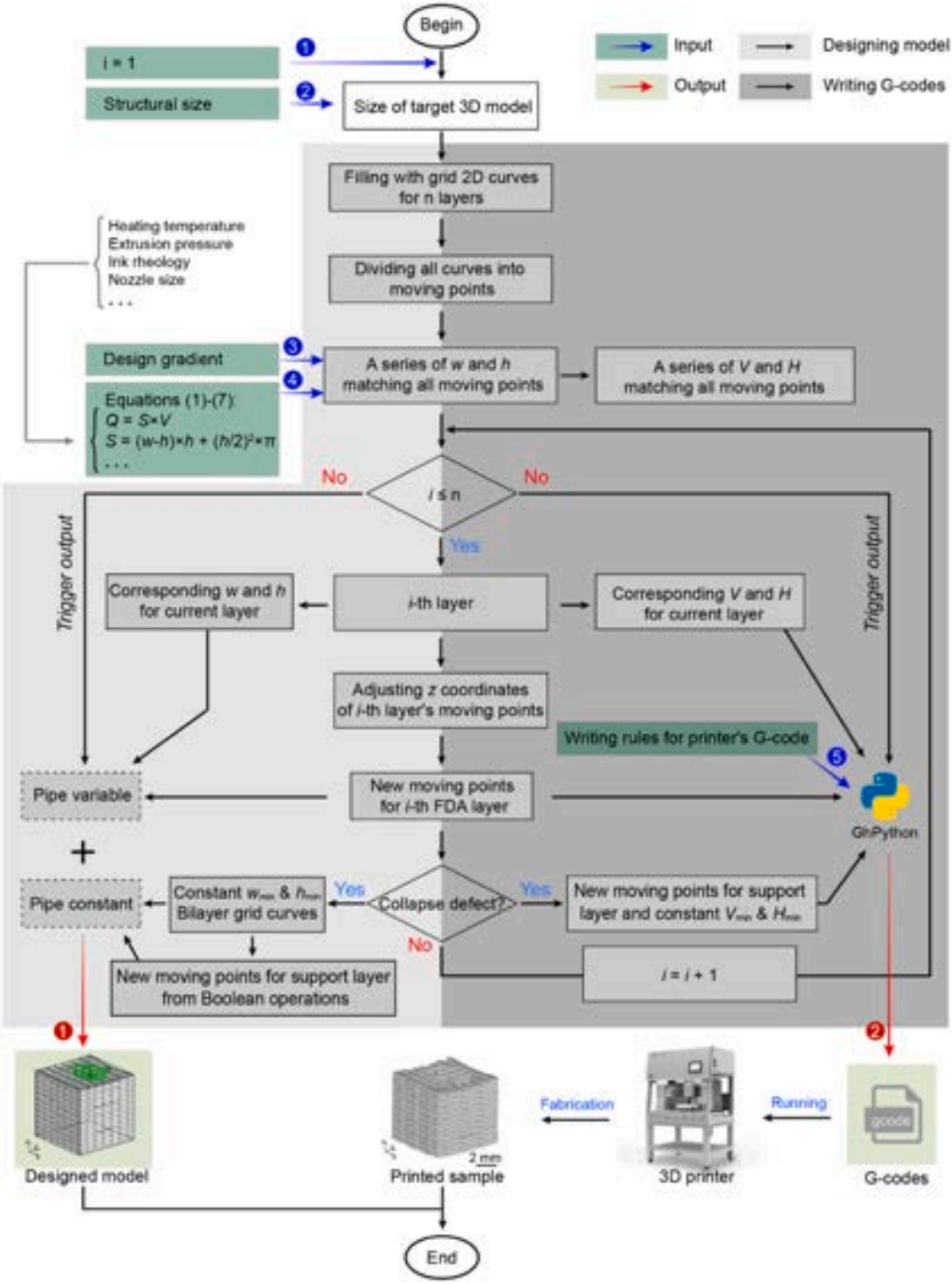

Fig. 9. Details of the HPD algorithm. The algorithm takes in five inputs (depicted by blue arrows) and yields two outputs (indicated by red arrows). Internal work instructions for this algorithm are represented by black arrows, categorized into designing the model (on the left side, light gray), collapse compensation (on the left and middle sides), and writing G-codes (on the right side, dark gray). The obtained G-code file was used for FDA-3D printing.

the collapse and bilayer trajectory curves (k-m). Although the operation result was not the empty set, the obtained printing trajectory (i.e., for supporting layers) for compensating the collapse was too short (< 3 mm). Hence, we deferred this collapse to the next layer for compensation. The top surface obtained in Step 2 was selected as a new substrate for the next layer (n).

Step 5. The closed curves of the second layer were panned onto the new substrate obtained in Step 4, as shown in (o-p). This step was similar to Step 1.

Step 6. The new collapse was obtained after moving the second layer, as shown in (q-s). This step was similar to Steps 2–3.

Step 7. Boolean intersection operation was repeated against the collapse of the second layer, as shown in (t-u). It was similar to Step 4. The operation result was two-layer trajectory curves, whose bottom

filaments (bottom layer) were long enough to be retained (> 3 mm) and the top filament (top layer) was too short to be discarded (< 3 mm). Eventually, the bottom filaments (i.e., supporting layer) were added for the collapse of the two-layer radial gradient pore model, as shown in (v). Notably, in the supporting layers, their filament cross-sectional sizes are constant minimum values (i.e., D_{min}, w_{min}, and h_{min}).

Step 8. After stacking the retained supporting layer filaments on the new substrate obtained in Step 4, the new top surface of the resulting model was obtained and used as the new substrate for the third layer (w).

2.9. Sample fabrication

The G-code files (*.gcode) generated by our proposed HPD algorithm (from sub-algorithm 3) were recognized and executed by the control software (3D Bio-Architect®) of our laboratory's commercial 3D printer (hardware platform, Regenovo Bio-Architect® WS, China). Further, motion commands were sent to the hardware platform to perform FDA-3D printing.

2.10. Filament cross-sectional width

To reduce experimental costs, we used a digital camera (Sony α7 II, Japan) to capture top-view photographs of single-filament samples, as presented in Fig. 3a. These photographs were imported into the ImageJ software (https://imagej.nih.gov/ij/). Then, the imported photographs were scaled, converted to grayscale format, and thresholded for segmentation. Finally, a series of widths (w) of the single-filament cross-section were obtained, as depicted in Fig. 3b.

2.11. Boolean operation

Notably, for obtaining the internal pore of the micro-CT reconstructed sample, we performed two-step Boolean operations, as depicted in Fig. 8. In the first step (Fig. 8a), the ~10×10×10 mm^3 cube created based on the outer contour of the sample was scaled in the x-y-z direction. Then, the scaled cube (~9×9×9 mm^3), named the region of interest (ROI), was subjected to a Boolean intersection with the reconstruction model of the fabricated sample. The input and output of the first step were displayed in Fig. 8d and e, respectively. In the second step (Fig. 8b), Boolean subtraction was performed between the ROI and sample materials, and the obtained pore structures in the ROI were illustrated in Fig. 8f. The pore image dataset obtained from the two-step Boolean operation was imported into the software ImageJ and then the pore size map was obtained using ImageJ's plug-in BoneJ (https://bonej.org/) [42].

2.12. Micro-CT imaging

The printed single-filament samples and heterostructure pore samples were imaged using a micro-CT scanner (SCANCO, Switzerland) with a resolution of 20 μm. The obtained micro-CT image dataset was processed and reconstructed using the Bruker software package including DataViewer and CT-Analyser (CTAn). First, the image dataset was rotated along the x-y-z direction using the software DataViewer to straighten the samples, and then the resulting images were exported. Second, using the software CTAn, the straightened images were thresholded and further were used to create 3D digital models of the scanned samples, as shown in Fig. 4b, Fig. 10, Fig. 8d-f, Fig. 18b, and Supplementary Fig. 2.

2.13. Filament cross section

The micro-CT images of single-filament samples were straightened using the software DataViewer. Then, the straightened images were thresholded and further exported as x-y plane images using the software CTAn. A series of x-y plane images were imported into the software ImageJ, and quantitative measurements were processed using the Batch Process tool to obtain the filament cross-sectional width (w), height (h), area (S), and aspect ratio (AR) (Fig. 5).

2.14. Pore and structure size evaluation

To quantitatively evaluate the internal pore size of the FDA-3D printed heterostructures, the following steps were performed. First, the printed samples were scanned using micro-CT equipment (SCANCO, Switzerland). Second, the micro-CT images were processed for straightening and threshold segmentation using the softwares DataViewer and CTAn, respectively. The processed image dataset was imported into ImageJ and then was scaled, thresholded, and booleaned. Finally, the pore size analysis was performed on the above image dataset using the plugin BoneJ (https://bonej.org/) [42], which resulted in 2D (in the x-y plane) images of pore size map with pseudo-colors. A series of 2D images in the z-axis direction were converted into the 3D image (model) of the pore size map using ImageJ's 3D Viewer command. Note that 2D images and 3D models of structure size maps (5th row, Fig. 10) could be obtained using the software BoneJ's Trabecular Thickness command based on the above operations.

3. Results and discussion

3.1. Overview of the HPD algorithm

Building upon FDA-3D printing technology [39], we developed the HPD algorithm utilizing the software platform Rhinoceros® and its tool Grasshopper® (United States). As an illustration, we chose a radial pore gradient within a cube to demonstrate the algorithm's capability in designing, visualizing, and fabricating heterogeneous pore structures. As shown in Fig. 1, the workflow of this study is delineated into five components: FDA-3D printing technology, HPD algorithm, designed model, customized G-codes, and printed sample. Notably, the HPD algorithm consists of three sub-algorithms: (1) model design, (2) collapse compensation, and (3) obtaining G-codes. These three sub-algorithms interconnect, ultimately producing the designed gradient model and its corresponding G-code file. Further details of the proposed HPD algorithm are provided in Fig. 9.

As shown in Fig. 9, the HPD algorithm has five input parameters (green area and blue arrow): the initial value of iterative parameters (i = 1), the structural size of the target model, the design gradient in pore sizes, the Equation basis for FDA-3D printing, and the writing rules for the available 3D printer's G-codes. The left and right shaded areas are the model design with collapse compensation (sub-algorithms 1 and 2) and the G-code generation (sub-algorithm 3), respectively. Notably, collapse compensation (sub-algorithm 2) is embedded in the model design (sub-algorithm 1) to produce gradient models with high fidelity.

3.2. Heterogeneous design

After initiating this algorithm, the preset commands were executed sequentially in the direction of the black arrows, and the commands for designing the FDA and supporting filaments were cycled until all FDA layers (n layers) were stacked. After the algorithm had run its course, the output command was triggered. The designed model was baked from Grasshopper® and then visualized in Rhinoceros®, and the customized G-code file was written using Grasshopper's built-in battery GhPython Script.

In the design and visualization of heterogeneous pore models (sub-algorithm 1), it is critical to establish the relationship between the design gradient in pore sizes and the cross-sectional sizes of filaments. In the context of FDA-3D printing, we initially investigated the impact of printing parameters on the filament deposition states (Fig. 3 and Supplementary Section 1, Supporting Information). The result showed that

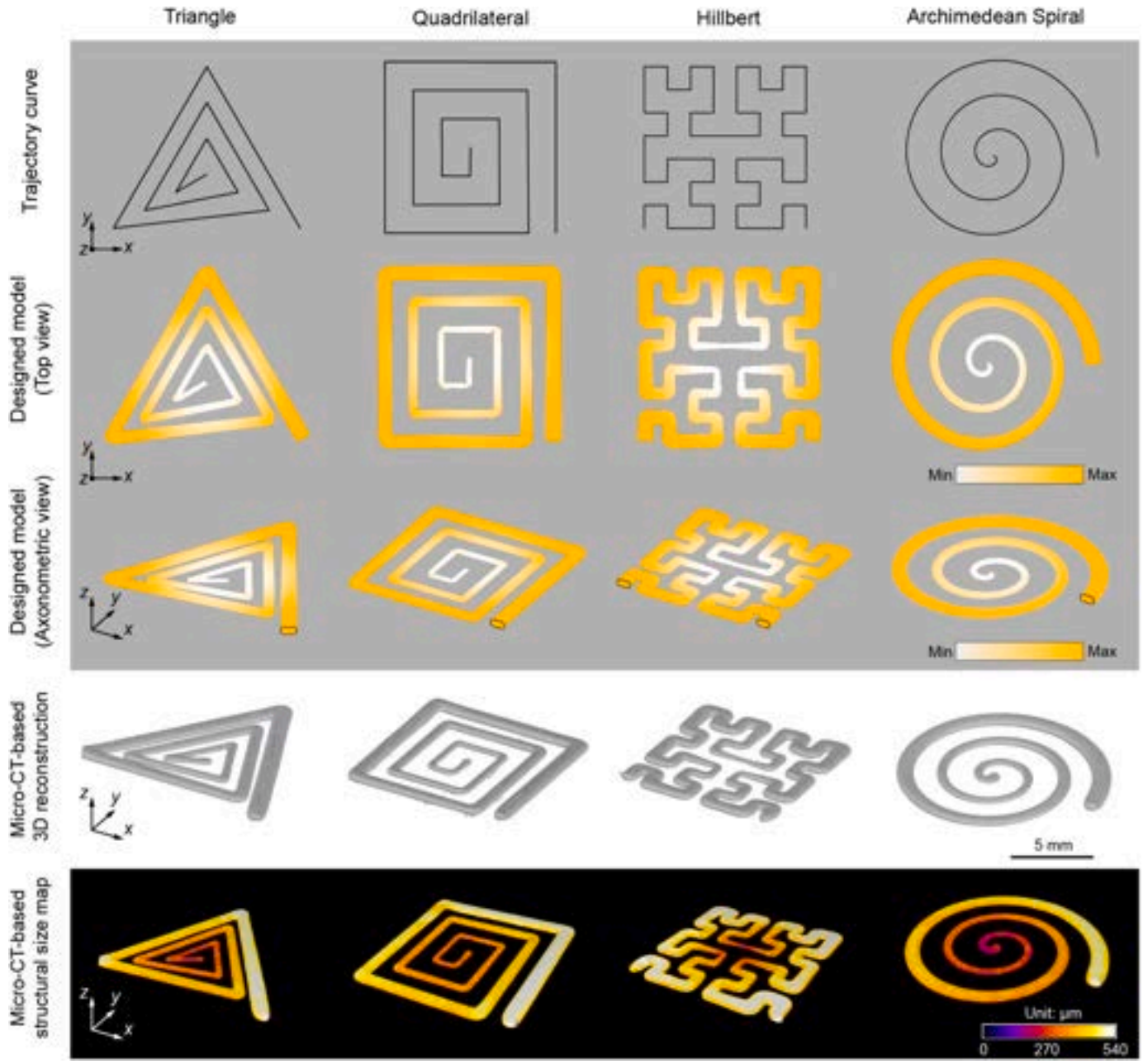

Fig. 10. Single-layer radial gradient porous matters with various infilling patterns. We demonstrated the design, fabrication, and evaluation of four heterogeneous matters, including triangle, quadrilateral, Hilbert, and Archimedean spiral. The trajectory curve, designed 3D model, micro-CT imaging, and structural size map are displayed. The pseudo-color represents the structural sizes of the designed models (2nd and 3rd rows) and fabricated samples (5th row).

maintaining the appropriate printing height (H) throughout the 3D printing process was crucial for achieving uniform straightness of the deposited filament. Our previous study [39] suggested that H was approximately 0.3–1.0 times the filament diameter D. While quantitative control of D could be achieved by adjusting both printing velocity (V) and extrusion air pressure (i.e., feeding flow rate, Fig. 3 and Supplementary Section 1, Supporting Information), a notable difference exists in their response times. Due to the stepper motors employed in this work, changes in V are typically executed in tens of milliseconds, or even less. However, given that air pumps operate with compressed air, changes in extrusion air pressure often require several seconds, which makes it difficult to achieve continuous variable control. Consequently, V was employed in this study for FDA-3D printing. It is noteworthy that this choice was constrained by our laboratory's pneumatic extrusion 3D printer (Regenovo Bio-Architect® WS). Given high-precision feeding with piston or screw drives [9,43], we posit that both feeding flow rate and V can be combined to produce FDA filaments on a broader scale.

Further, we investigated the relationship between V and the filament cross-sectional sizes. To qualitatively (Fig. 4) and quantitatively (Fig. 5) evaluate their relationship, we designed a 50 mm-long printing path with a uniform variation in velocity ranging from 2 mm s^{-1} to 14 mm s^{-1}. The cross-section images revealed that the filament's cross-sectional shape was approximately oblong [44,45]. Therefore, we introduced the filament cross-sectional width (w), height (h), area (S), and aspect ratio (AR) to define its sizes (*Algorithmic foundation* in Material and Methods). We performed fittings for S and AR, resulting in Eqs. 4 and 5 (Fig. 5), respectively. The fitting result for S was in good agreement with its theoretical counterpart derived through fluid flow [7]. Note that this strategy relies on the printing velocity to control the aperture and print result. Although this can be accomplished by

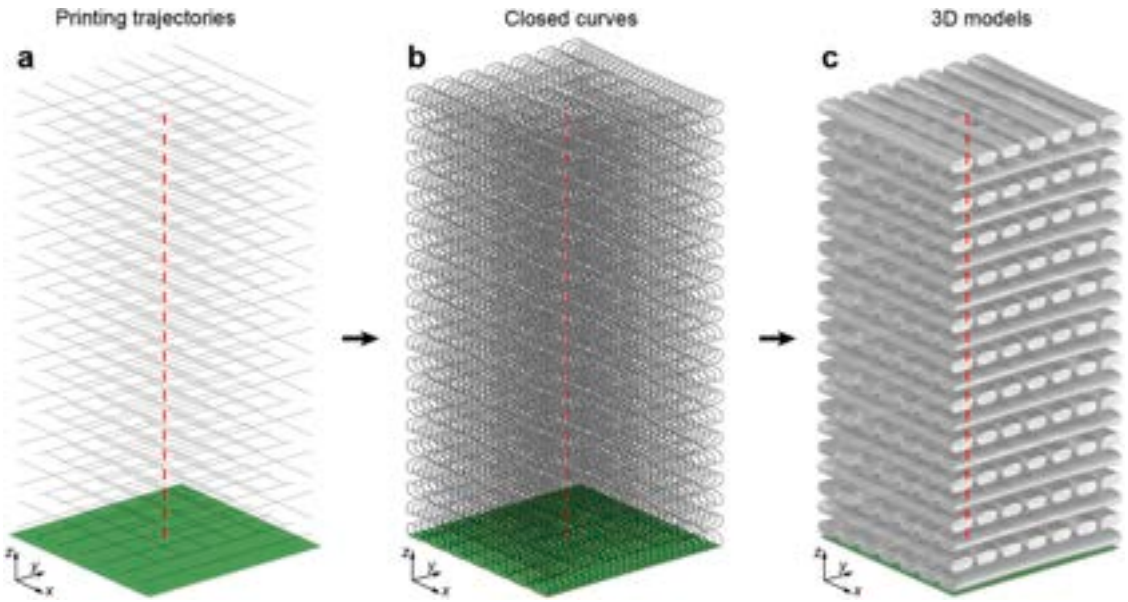

Fig. 11. Design of the multi-layer model before stacking. (a) Original printing trajectories of FDA layers. (b) Closed curves of FDA layers with variable *w* and *h*. (c) FDA multi-layer 3D models. The total number of FDA layers is 22. The red dashed line is the radial interference element in a 10×10×10 mm^3 cube. Pore sizes were determined by the distance from their geometric center to the red dotted line.

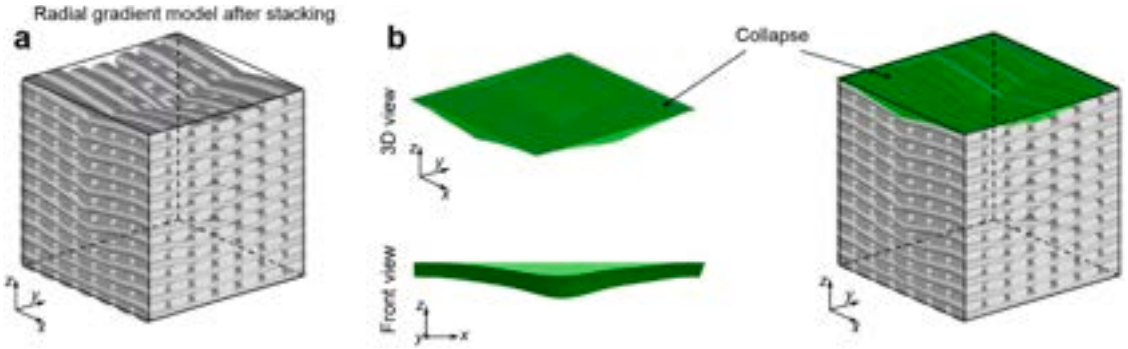

Fig. 12. Multi-layer model showing collapse. (a) Radial gradient 3D model after stacking FDA layer of 22 filaments. (b) Collapse obtained by subtracting the radial gradient 3D model from the 10×10×10 mm^3 cube.

specifying the printing velocity in the G-code, the printer firmware adjusts the printing velocity at corners based on the maximum acceleration. As a result, this method works well for straight trajectories without corners, but corner printing must still be approached with caution [46]. In this paper we set the printing velocity at the corners to the maximum of the printing velocity range (14 mm s^{-1}).

Based on the relationship between *V* and filament cross-sectional size (Eqs. 2–5), we further established the relationship between the gradient in pore sizes and the printing parameters (Fig. 6, *Heterogeneous pore design* in Material and Methods; Supplementary Fig. 3, Supplementary Information). To demonstrate the generalizability of our proposed HPD algorithm (Fig. 9), we designed, fabricated, and evaluated single-layer filaments with diverse infill patterns. The results showed a consistent radial gradient in pore sizes, aligning with the intended design specifications (Fig. 10).

3.3. Support generation for collapse prevention

Repeating the design for an FDA single-layer filament model resulted in a multi-layer model (Fig. 11 and Supplementary Section 3, Supporting Information). All FDA layers (main layers) were sequentially stacked together one by one along the *z*-axis to simulate the 3D printing deposition. Notably, a collapse is observed at the top center region of the resulting model (Fig. 12). To address this issue, the collapse compensation (sub-algorithm 2) was introduced to selectively add supporting layers with constant *D* filaments at collapse locations through Boolean intersection operations. Compensation for an FDA two-layer filament model was selected as an example to illustrate the operational steps in this sub-algorithm (Fig. 7, *Support generation for collapse prevention* in Material and Methods).

The multi-layer model with collapse compensation and corresponding printing trajectories (Fig. 13a) and *V* (Fig. 13b) were obtained after stacking all FDA and supporting layers one by one. To quantitatively assess the extent of the local collapse of the designed model, we individually identified 121 continuous points on the top surface and horizontal plane following the stacking of filaments in a given layer (Fig. 14). Quantitative results displayed that the groups without and with collapse compensation exhibited extents of up to 1.75 mm and less than 0.75 mm, respectively (Fig. 15). It can be concluded that sub-algorithm 2 effectively enhanced the geometry fidelity of the designed model. Therefore, integrating the collapse compensation (sub-algorithm 2) into the model design (sub-algorithm 1) proved to be an effective strategy for mitigating defects in heterogeneous materials (Fig. 9).

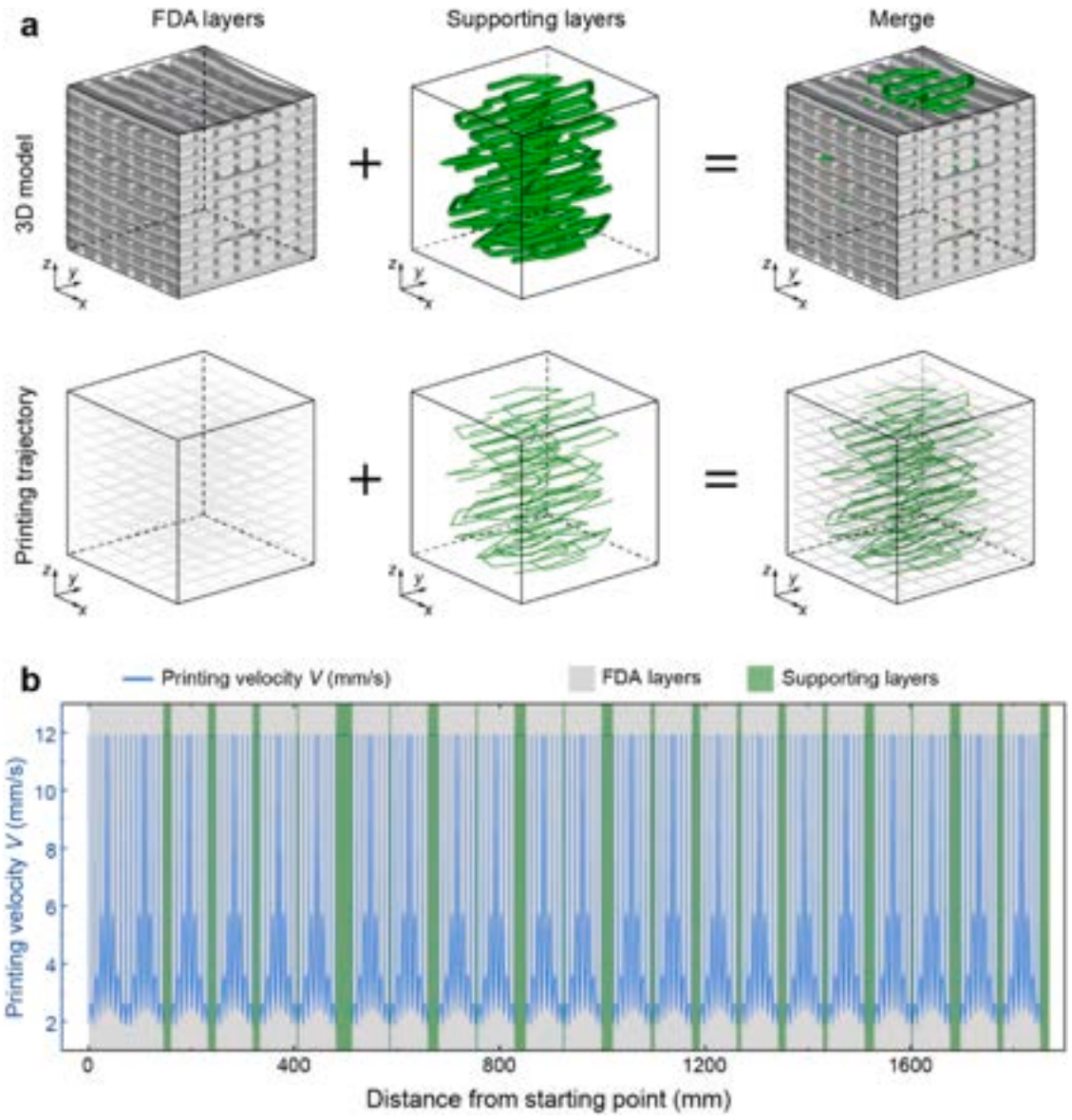

Fig. 13. (a) Multi-layer filament 3D model with the radial gradient and its printing trajectory in a 10×10×10 mm cube. It consists of 22 FDA layers and 21 supporting layers. The FDA layers have variable cross-sectional sizes, while the supporting layers maintain constant sizes. The FDA and supporting layers are stacked by index, as are the printing trajectory and the printing velocity *V*. (b) Plotting of a series of printing velocities *V* for the radial gradient structure.

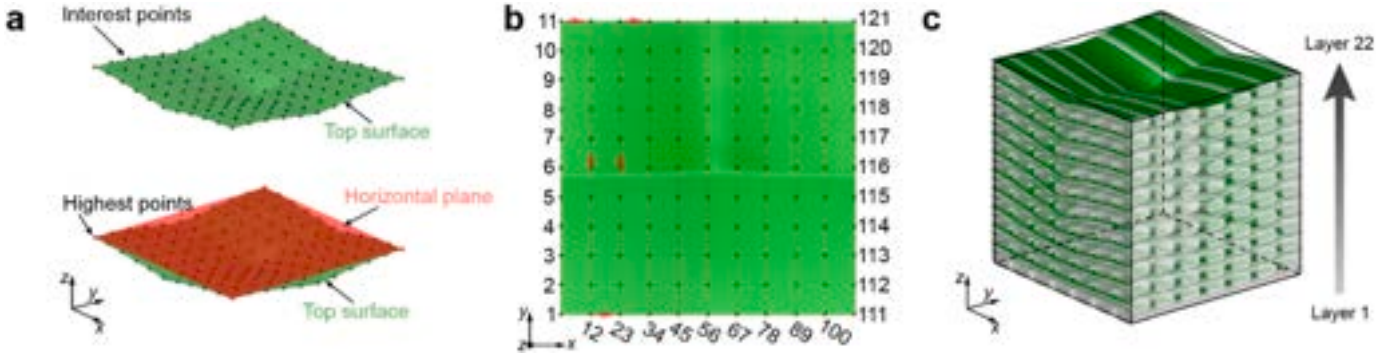

Fig. 14. A quantitative method for evaluating the degree of collapse during the design of gradient porous models. (a) Creating the top surface (green) and horizontal plane (red) for the heterogeneous model in Fig. 12a. (b) Dividing the created top surface and horizontal plane into 121 points of interest along the grid path (red arrows), respectively. Each numbered point on the top surface and the horizontal plane has the same *xy* coordinates, but different *z* coordinates. A series of vertical distances between all corresponding numbered points were used to quantify the degree of collapse. (c) Top surfaces after stacking each FDA layer.

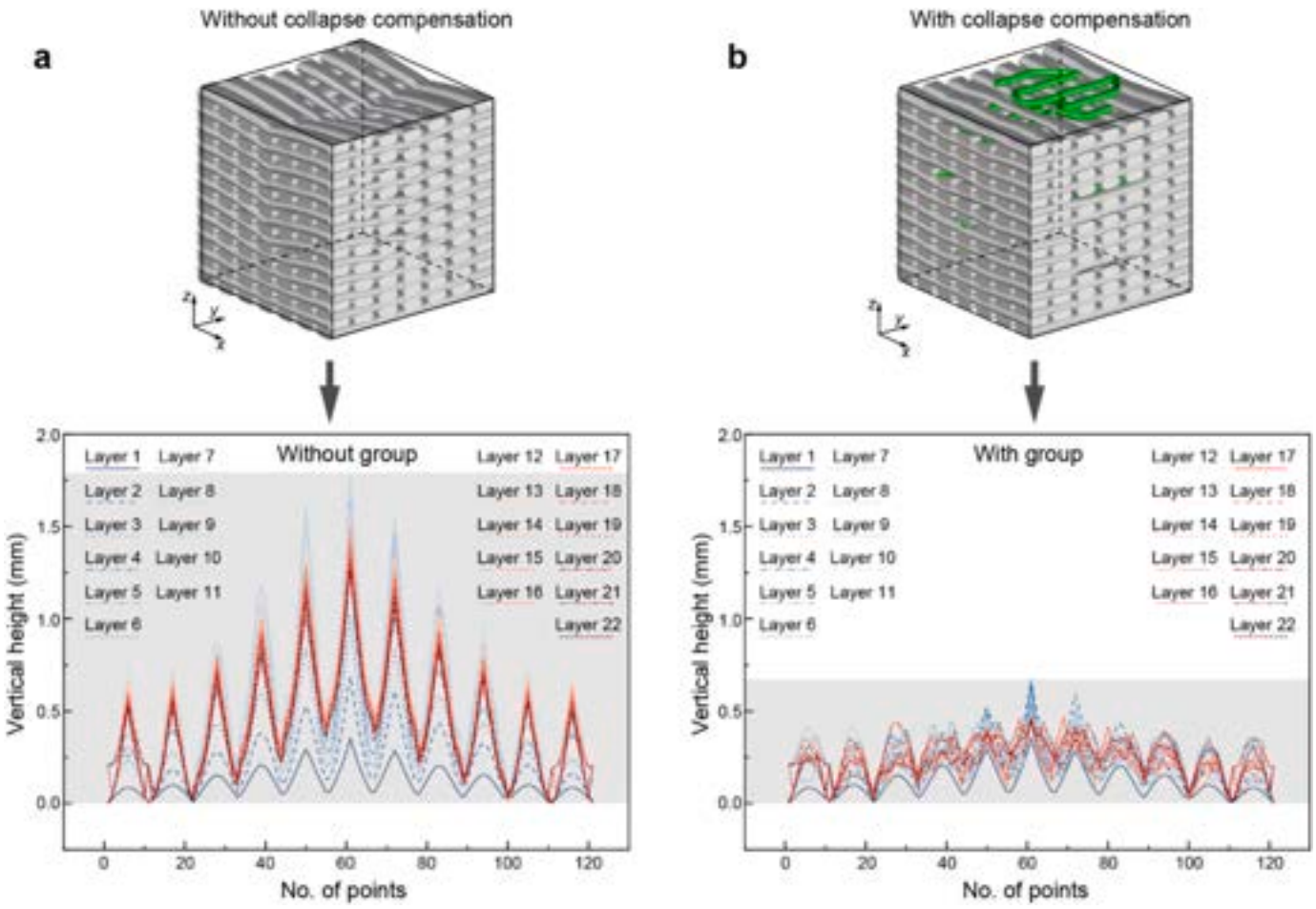

Fig. 15. Quantitative evaluations of radial gradient pore models without (a) and with (b) collapse compensation. The bottom sub-figures show the degree of collapse at different points of interest after all FDA layers are stacked sequentially. These points of 121 make up a continuous grid fill line, as defined in Fig. 14a-b. Vertical heights (fluctuation bands, gray region) in the with collapse compensation group were significantly smaller than those in the without collapse compensation group.

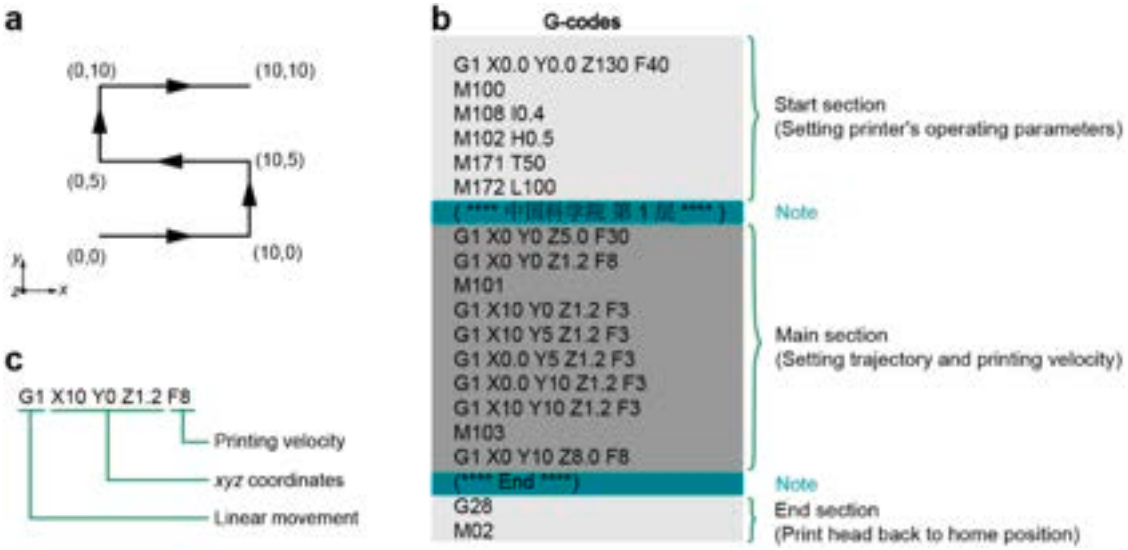

Fig. 16. Definition and writing rules for G-codes.(a) An example of a printing trajectory in the *x-y* plane. (b) Details of the G-code file corresponding to the example trajectory in (a). (c) Single line code for linear movement.

3.4. G-code generation

During extrusion printing, the print head with one or more nozzles is controlled and moved by G-code files to deposit inks along a pre-determined trajectory, operating under defined working conditions. To produce the heterogeneous models designed using sub-algorithms 1 and

Pseudocode for writing G-code files in GhPython Script

Input : File path, G-code rules, work situation,
The i-th points for FDA lines with variable nozzle height, $\boldsymbol{pts_i}$
Printing velocity corresponding to the moving point, $\boldsymbol{V_i}$
FDA lines for scaffold model, $\boldsymbol{line_j}$
Number of points for every FDA line, **N_pts**
Number of lines on every FDA layer, **N_line**
Number of FDA layers, **N_layer**
Boolean for if support is needed, $\boldsymbol{Bool_k}$
Number of lines on the k-th supporting layer, $\boldsymbol{N\_line_k}$
Number of points for the m-th supporting line on the k-th supporting layer, $\boldsymbol{N\_pts\_sup_{k,m}}$
The n-th point for the m-th supporting line on the k-th supporting layer, $\boldsymbol{pts\_sup_{k,m,n}}$

Output: G-codes, *.gcodes

Range: $i \in [0, \text{N\_pts}*\text{N\_line}*\text{N\_layer}]$, $j \in [0, \text{N\_line}*\text{N\_layer}]$
$k \in [0, \text{N\_layer}]$, $m \in \mathbb{N}$, $n \in \mathbb{N}$, N_pts = 26, N_line = 7, N_layer = 22

```
Initializing extrusion 3D printer (Start section)
for i pts_i in all points of FDA lines do                                   i←0
    if i % N_pts == 0 then                                                  j←0, N_line←7
        if j line_j % N_line == 0 then                                      k←0
            k = k + 1;
        G1 pts_ix, pts_iy, (pts_iz+5), F30;
        G1 pts_ix, pts_iy, pts_iz, F5;
        M101;
        j = j + 1
    elif (i+1) % N_pts == 0 then
        G1 pts_ix, pts_iy, pts_iz, FV_i;
    else
        M103;
        G1 pts_ix, pts_iy, pts_iz, FV_i;
        G1 pts_ix, pts_iy, (pts_iz+5), F5;
        if (j line_j % N_line == 0) AND (Bool_k == 0) then                  k←k-1
            for k, m, n pts_sup_k,m,n in all points of supporting lines do  k←k-1, m, n←0
                if n % N_pts_sup_k,m == 0 then
                    G1 pts_ix, pts_iy, (pts_iz+5), F30;
                    G1 pts_ix, pts_iy, pts_iz, F5;
                    M101;
                    n = n + 1
                else
                    G1 pts_ix, pts_iy, pts_iz, FV_min;                      V_min←2.0
                    n = n + 1
                    if n % N_pts_sup_k,m == 0 then
                        M103;
                        G1 pts_ix, pts_iy, (pts_iz+5), F5;
                        n = 0
                        if m < (N_line_k -1) then
                            m = m + 1
                        else
                            m = m
            end for
    i = i + 1
end for
Nozzle return to home position (End section)
```

Fig. 17. Pseudocode for writing G-code files (Sub-algorithm 3). Regular and italic symbols indicate a constant value and a data set, respectively.

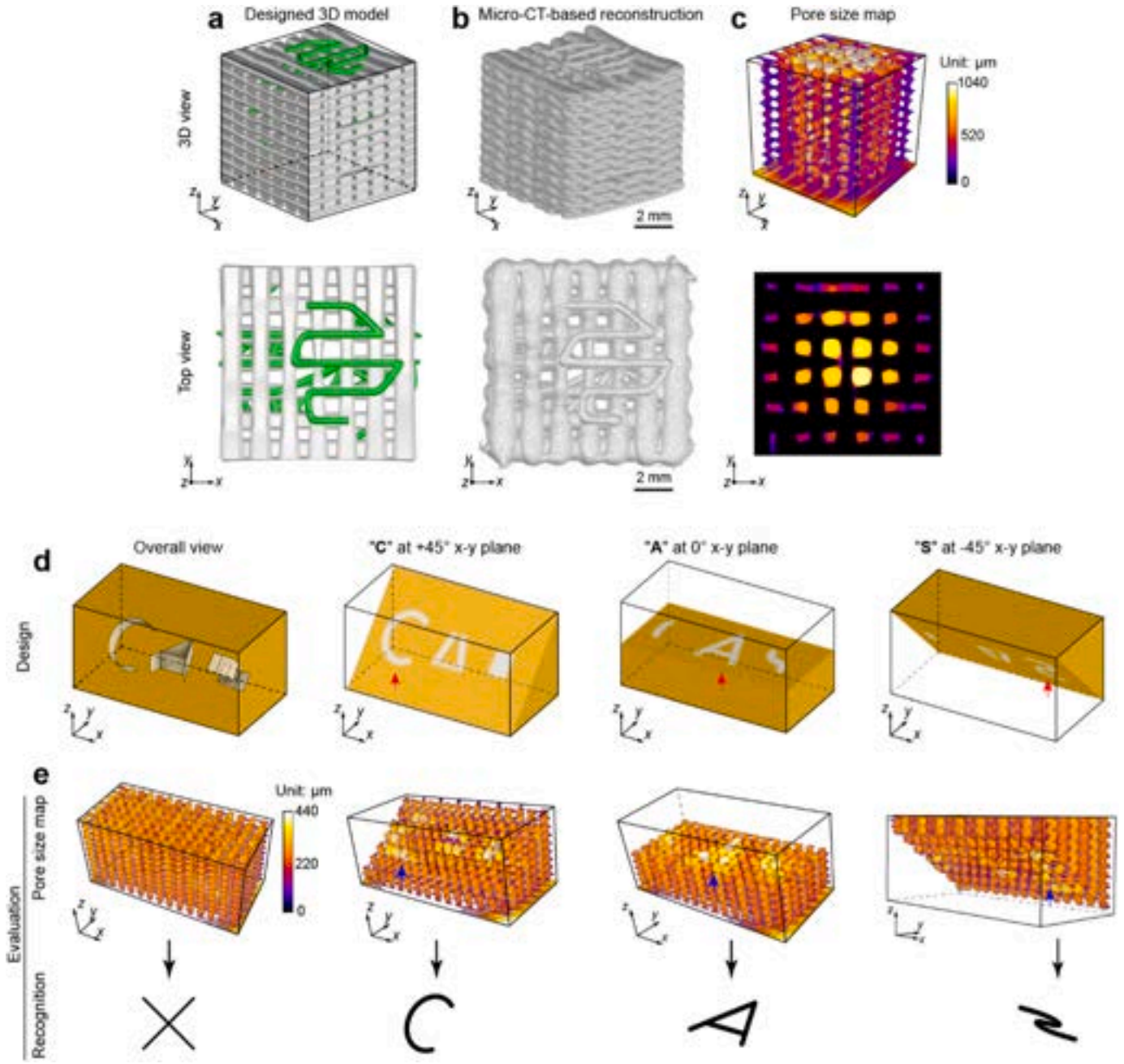

Fig. 18. Heterogeneous matters with radial gradient and letter-embedded gradient in pore sizes.(a-c) Design, reconstruction, and quantification of radial-gradient heterogeneous matter. In (a), Gray, FDA layers; green, supporting layers. In (b), model reconstruction was performed based on micro-CT images, and the scale bar is 2 mm. In (c), the top (3D view) and bottom (top view) sub-figures correspond to each other. The black in the bottom sub-figure indicates the PCL/β-TCP structural material, corresponding to the blank in the top sub-figure. The colored map shows a radial gradient in pore sizes ranging from 0 to 1040 μm. (d-e) Design and evaluation of CAS (abbreviation for Chinese Academy of Sciences) letters-embedded heterogeneous matter. Two different pore sizes were designed for letter and non-letter regions respectively. In (d), red arrows mark the position of CAS letters in the designed model. The micro-CT reconstruction was subjected to the two-step Boolean operation and then analyzed using the software ImageJ to obtain the pore size map. In (e), blue arrows mark the position of CAS letters in the pore size map. The cross (×) indicates that no letters could be observed. The letters 'C', 'A', and 'S' were located in the +45°, 0°, and −45° *x*-*y* planes after slicing, respectively.

2, G-code files were used as an intermediary between model design and FDA-3D printing. The writing rules for our available printer's G-code files are detailed in Fig. 16. Subsequently, a G-code acquisition sub-algorithm (referred to as sub-algorithm 3) was developed using the GhPython Script battery in Grasshopper® (5th input, Fig. 9), and its pseudocode was shown in Fig. 17. Once the heterogeneous pore models designed by sub-algorithms 1 and 2 met the gradient requirements, sub-algorithm 3 was activated. It would generate all the moving points (printing trajectory, Fig. 13a) and corresponding *V* (Fig. 13b), which were then compiled into G-code files executable by our 3D printer. The interconnected details of the three sub-algorithms in the HPD algorithm are elaborated upon in Fig. 1 and Fig. 9.

3.5. Applications of the HPD algorithm

Utilizing our proposed HPD algorithm, we designed a radial gradient pore model incorporating FDA (gray) and supporting (greener) layers (Fig. 18a) and generated the corresponding G-code file. The actual

samples were manufactured using our laboratory's commercial single-nozzle material extrusion-based 3D printer (Regenovo Bio-Architect® WS, China) by executing the customized G-code file. Subsequently, they were scanned and 3D reconstructed as depicted in Fig. 18b. The imaging result demonstrated an exceptionally high fidelity between the design and reconstruction models, confirmed through both the 3D view and the top view.

Ultimately, after a two-step Boolean operation (Fig. 8, *Boolean operation* in Material and Methods), we conducted a qualitative and quantitative assessment of the pore sizes inside the fabricated sample using ImageJ software and its BoneJ plug-in based on micro-CT images. As shown in Fig. 18c and Supplementary Fig. 1, the pore size result revealed that the pore size distribution exhibited a radial gradient.

Additionally, we designed, fabricated, and evaluated a heterogeneous pore structure embedded with CAS letters (abbreviation for Chinese Academy of Sciences), as illustrated in Fig. 18d-e and Supplementary Fig. 2. The letters 'C', 'A', and 'S' were positioned in the $+45°$, $0°$, and $-45°$ *x-y* planes, respectively. Micro-CT imaging revealed that the fabricated sample did not experience collapse and exhibited homogeneous pore structures before slicing (Fig. 18e, overall view). Interestingly, the pore size map result showed that the CAS letters could be respectively observed after slicing along the three planes ($+45°$, $0°$, and $-45°$ *x-y* planes), as depicted in Fig. 18e. These two applications demonstrated the viability of our proposed HPD algorithm for FDA-3D printing of heterogeneous porous matters. Currently, material extrusion AM technology has been widely used in the field of bio-printing, due to its advantages such as simple equipment, cell-friendly, and extensive availability of biomaterials. Bio-printing in controlled morphology kidney-like organs showed an effect on epithelial formation and functional expression [47]. Our proposed HPD algorithm has the potential to improve the capability of material extrusion-based bio-printing.

4. Conclusion

In this study, we have proposed the HPD algorithm for the design, visualization, and FDA-3D printing of heterogeneous pore structures, utilizing the software Rhinoceros® and its plug-in Grasshopper®. This algorithm allows us to design complex porous models with highly tunable gradients and without collapse, and to upgrade extrusion-based 3D printers to fabricate the designed heterogeneous models. Micro-CT-based 3D reconstruction and pore size map results show the outstanding performance and multiple capabilities of this algorithm in creating heterogeneous porous structures inside matters. Overall, our proposed HPD algorithm demonstrates the enhanced capability of material extrusion 3D printing technology in creating complex functionally gradient porous structures/materials, showing a great potential to rejuvenate a substantial number of extrusion printers without additional equipment replacement costs.

CRediT authorship contribution statement

Kaizheng Liu: Writing – review & editing, Visualization, Validation. **Juan Liu:** Writing – review & editing, Supervision, Resources, Methodology. **Huawei Qu:** Writing – review & editing, Writing – original draft, Visualization, Validation, Project administration, Methodology, Investigation, Funding acquisition, Data curation, Conceptualization. **Chongjian Gao:** Writing – review & editing, Visualization, Methodology, Data curation. **Changshun Ruan:** Supervision, Project administration, Funding acquisition.

Declaration of Competing Interest

The authors declare that they have no known competing financial interests or personal relationships that could have appeared to influence the work reported in this paper.

Data availability

Data will be made available on request.

Acknowledgments

This work was supported by the National Key R&D Program of China (Grant No. 2022YFA1207502), the National Natural Science Foundation of China (Grant Nos. 32122046, 82072082, and 32201097), the China Postdoctoral Science Foundation (Grant No. 2023M733668), and Shenzhen International Science and Technology Cooperation Project (Grant No. GJHZ20240218112602004).

Appendix A. Supporting information

Supplementary data associated with this article can be found in the online version at doi:10.1016/j.addma.2024.104449.

References

[1] U.G.K. Wegst, H. Bai, E. Saiz, A.P. Tomsia, R.O. Ritchie, Bioinspired structural materials, Nat. Mater. 14 (1) (2015) 23–36.
[2] S. Feng, P. Zhu, H. Zheng, H. Zhan, C. Chen, J. Li, L. Wang, X. Yao, Y. Liu, Z. Wang, Three-dimensional capillary ratchet-induced liquid directional steering, Science 373 (6561) (2021) 1344–1348.
[3] S.L. Wu, X.M. Liu, K.W.K. Yeung, C.S. Liu, X.J. Yang, Biomimetic porous scaffolds for bone tissue engineering, Mater. Sci. Eng. R. -Rep. 80 (2014) (2014) 1–36.
[4] N. Reznikov, M. Bilton, L. Lari, M.M. Stevens, R. Kröger, Fractal-like hierarchical organization of bone begins at the nanoscale, Science 360 (6388) (2018) eaao2189.
[5] L. Yi, M. Glatt, S. Ehmsen, W. Duan, J.C. Aurich, Process monitoring of economic and environmental performance of a material extrusion printer using an augmented reality-based digital twin, Addit. Manuf. 48 (2021) 102388.
[6] M.A. Skylar-Scott, J. Mueller, C.W. Visser, J.A. Lewis, Voxelated soft matter via multimaterial multinozzle 3D printing, Nature 575 (7782) (2019) 330–335.
[7] S. Duraivel, D. Laurent, D.A. Rajon, G.M. Scheutz, A.M. Shetty, B.S. Sumerlin, S. A. Banks, F.J. Bova, T.E. Angelini, A silicone-based support material eliminates interfacial instabilities in 3D silicone printing, Science 379 (6638) (2023) 1248–1252.
[8] Z. Jiang, B. Diggle, M.L. Tan, J. Viktorova, C.W. Bennett, L.A. Connal, Extrusion 3D printing of polymeric materials with advanced properties, Adv. Sci. 7 (17) (2020) 2001379.
[9] Y.S. Zhang, G. Haghiashtiani, T. Hübscher, D.J. Kelly, J.M. Lee, M. Lutolf, M. C. McAlpine, W.Y. Yeong, M. Zenobi-Wong, J. Malda, 3D extrusion bioprinting, Nat. Rev. Method. Prim. 1 (1) (2021) 75.
[10] G. Fang, T. Zhang, S. Zhong, X. Chen, Z. Zhong, C.C.L. Wang, Reinforced FDM: multi-axis filament alignment with controlled anisotropic strength, ACM Trans. Graph. 39 (6) (2020) 204.
[11] T. Zhang, G. Fang, Y. Huang, N. Dutta, S. Lefebvre, Z.M. Kilic, C.C.L. Wang, S3-slicer: a general slicing framework for multi-axis 3D printing, ACM Trans. Graph. 41 (6) (2022) 277.
[12] Y. Hui, Y. Yao, Q. Qian, J. Luo, H. Chen, Z. Qiao, Y. Yu, L. Tao, N. Zhou, Three-dimensional printing of soft hydrogel electronics, Nat. Electron. 5 (12) (2022) 893–903.
[13] F. Kim, S.E. Yang, H. Ju, S. Choo, J. Lee, G. Kim, S.-h Jung, S. Kim, C. Cha, K. T. Kim, S. Ahn, H.G. Chae, J.S. Son, Direct ink writing of three-dimensional thermoelectric microarchitectures, Nat. Electron. 4 (8) (2021) 579–587.
[14] A. Kotikian, C. McMahan, E.C. Davidson, J.M. Muhammad, R.D. Weeks, C. Daraio, J.A. Lewis, Untethered soft robotic matter with passive control of shape morphing and propulsion, Sci. Robot. 4 (33) (2019) eaax7044.
[15] R. Tognato, A.R. Armiento, V. Bonfrate, R. Levato, J. Malda, M. Alini, D. Eglin, G. Giancane, T. Serra, A stimuli-responsive nanocomposite for 3D anisotropic cell-guidance and magnetic soft robotics, Adv. Funct. Mater. 29 (9) (2019) 1804647.
[16] E. Sachyani Keneth, A. Kamyshny, M. Totaro, L. Beccai, S. Magdassi, 3D printing materials for soft robotics, Adv. Mater. 33 (19) (2021) 2003387.
[17] T.J. Jones, E. Jambon-Puillet, J. Marthelot, P.T. Brun, Bubble casting soft robotics, Nature 599 (7884) (2021) 229–233.
[18] Z. Zhu, D.W.H. Ng, H.S. Park, M.C. McAlpine, 3D-printed multifunctional materials enabled by artificial-intelligence-assisted fabrication technologies, Nat. Rev. Mater. 6 (1) (2021) 27–47.
[19] K. De France, Z. Zeng, T. Wu, G. Nyström, Functional materials from nanocellulose: utilizing structure–property relationships in bottom-up fabrication, Adv. Mater. 33 (28) (2021) 2000657.
[20] S. Zhao, G. Siqueira, S. Drdova, D. Norris, C. Ubert, A. Bonnin, S. Galmarini, M. Ganobjak, Z. Pan, S. Brunner, G. Nyström, J. Wang, M.M. Koebel, W.J. Malfait, Additive manufacturing of silica aerogels, Nature 584 (7821) (2020) 387–392.
[21] H. Hwangbo, H. Lee, E.J. Roh, W. Kim, H.P. Joshi, S.Y. Kwon, U.Y. Choi, I.-B. Han, G.H. Kim, Bone tissue engineering via application of a collagen/hydroxyapatite 4D-printed biomimetic scaffold for spinal fusion, Appl. Phys. Rev. 8 (2) (2021) 021403.

[22] K. Liu, N. Hu, Z. Yu, X. Zhang, H. Ma, H. Qu, C. Ruan, 3D printing and bioprinting in urology, Int. J. Bioprinting 9 (6) (2023) 0969.
[23] H. Qu, H. Fu, Z. Han, Y. Sun, Biomaterials for bone tissue engineering scaffolds: a review, RSC Adv. 9 (45) (2019) 26252–26262.
[24] Z. Li, S. Li, C. Gao, J. Liu, H. Qu, J. Yang, W.W. Lu, C. Ruan, X. Niu, Continuous manufacturing of bioinspired bone-periosteum integrated scaffold to promote bone regeneration, Adv. Funct. Mater. n/a (n/a) (2024) 2403235.
[25] Q. Wan, W. Yang, L. Wang, G. Ma, Global continuous path planning for 3D concrete printing multi-branched structure, Addit. Manuf. 71 (2023) 103581.
[26] Y.W.D. Tay, J.H. Lim, M. Li, M.J. Tan, Creating functionally graded concrete materials with varying 3D printing parameters, Virtual Phys. Prototyp. 17 (3) (2022) 662–681.
[27] D. Chen, Q. Liu, Z. Han, J. Zhang, H. Song, K. Wang, Z. Song, S. Wen, Y. Zhou, C. Yan, Y. Shi, 4D printing strain self-sensing and temperature self-sensing integrated sensor–actuator with bioinspired gradient gaps, Adv. Sci. N./a(N./a (2020) 2000584.
[28] A. Ding, O. Jeon, R. Tang, Y.B. Lee, S.J. Lee, E. Alsberg, Cell-laden multiple-step and reversible 4D hydrogel actuators to mimic dynamic tissue morphogenesis, Adv. Sci. 8 (9) (2021) 2004616.
[29] J.J. Nijdam, D. Agarwal, B.S. Schon, An experimental assessment of filament-extrusion models used in slicer software for 3D food-printing applications, J. Food Eng. 317 (2022) 110711.
[30] D. Xie, H. Hu, Q. Huang, X. Lu, Influence of oleogel/hydrogel ratios and emulsifiers on structural and digestion properties of food-grade 3D printed bigels as carriers for quercetin and catechin, Food Hydrocoll. 144 (2023) 108948.
[31] T.C.R. Outrequin, C. Gamonpilas, W. Siriwatwechakul, P. Sreearunothai, Extrusion-based 3D printing of food biopolymers: a highlight on the important rheological parameters to reach printability, J. Food Eng. 342 (2023) 111371.
[32] S.D. Lacey, D.J. Kirsch, Y. Li, J.T. Morgenstern, B.C. Zarket, Y. Yao, J. Dai, L. Q. Garcia, B. Liu, T. Gao, S. Xu, S.R. Raghavan, J.W. Connell, Y. Lin, L. Hu, Extrusion-based 3D printing of hierarchically porous advanced battery electrodes, Adv. Mater. 30 (12) (2018) 1705651.
[33] H. Qu, Z. Han, Z. Chen, L. Tang, C. Gao, K. Liu, H. Pan, H. Fu, C. Ruan, Fractal design boosts extrusion-based 3D printing of bone-mimicking radial-gradient scaffolds, Research 2021 (2021) 9892689.
[34] P. Wu, K.S. Ramani, C.E. Okwudire, Accurate linear and nonlinear model-based feedforward deposition control for material extrusion additive manufacturing, Addit. Manuf. 48 (2021) 102389.
[35] M.P. Serdeczny, R. Comminal, D.B. Pedersen, J. Spangenberg, Experimental validation of a numerical model for the strand shape in material extrusion additive manufacturing, Addit. Manuf. 24 (2018) 145–153.
[36] A. Moetazedian, A.S. Budisuharto, V.V. Silberschmidt, A. Gleadall, CONVEX (CONtinuously Varied EXtrusion): a new scale of design for additive manufacturing, Addit. Manuf. 37 (2021) 101576.
[37] L. Grigolato, S. Rosso, R. Meneghello, G. Concheri, G. Savio, Design and manufacturing of graded density components by material extrusion technologies, Addit. Manuf. 57 (2022) 102950.
[38] T. Kuipers, E.L. Doubrovski, J. Wu, C.C.L. Wang, A framework for adaptive width control of dense contour-parallel toolpaths in fused deposition modeling, Comput. -Aided Des. 128 (2020) 102907.
[39] H. Qu, C. Gao, K. Liu, H. Fu, Z. Liu, P.H.J. Kouwer, Z. Han, C. Ruan, Gradient matters via filament diameter-adjustable 3D printing, Nat. Commun. 15 (2024) 2930.
[40] M.A.S.R. Saadi, A. Maguire, N.T. Pottackal, M.S.H. Thakur, M.M. Ikram, A.J. Hart, P.M. Ajayan, M.M. Rahman, Direct ink writing: a 3D printing technology for diverse materials, Adv. Mater. 34 (28) (2022) 2108855.
[41] R.D. Weeks, R.L. Truby, S.G.M. Uzel, J.A. Lewis, Embedded 3D printing of multimaterial polymer lattices via graph-based print path planning, Adv. Mater. 35 (5) (2023) 2206958.
[42] R. Domander, A.A. Felder, M. Doube, BoneJ2 - refactoring established research software, Wellcome Open Res 6 (2021) 37.
[43] J. Lai, C. Wang, M. Wang, 3D printing in biomedical engineering: processes, materials, and applications, Appl. Phys. Rev. 8 (2) (2021) 021322.
[44] R. Comminal, M.P. Serdeczny, D.B. Pedersen, J. Spangenberg, Numerical modeling of the strand deposition flow in extrusion-based additive manufacturing, Addit. Manuf. 20 (2018) 68–76.
[45] Y. Rao, N. Wei, S. Yao, K. Wang, Y. Peng, A process-structure-performance modeling for thermoplastic polymers via material extrusion additive manufacturing, Addit. Manuf. 39 (2021) 101857.
[46] R. Comminal, M.P. Serdeczny, D.B. Pedersen, J. Spangenberg, Motion planning and numerical simulation of material deposition at corners in extrusion additive manufacturing, Addit. Manuf. 29 (2019) 17.
[47] K.T. Lawlor, J.M. Vanslambrouck, J.W. Higgins, A. Chambon, K. Bishard, D. Arndt, P.X. Er, S.B. Wilson, S.E. Howden, K.S. Tan, F. Li, L.J. Hale, B. Shepherd, S. Pentoney, S.C. Presnell, A.E. Chen, M.H. Little, Cellular extrusion bioprinting improves kidney organoid reproducibility and conformation, Nat. Mater. 20 (2) (2021) 260–271.